POLITECNICO DI MILANO
School of Industrial and Information Engineering
Master of Science in Materials Engineering and Nanotechnology

Flow sensor based on a twin optical fiber interferometer

Supervisor: Prof. Stefano Mariani
Co-Supervisor: Prof. Sabina Merlo

Candidate:
Tiago Vicentini Ferreira do Valle
Matriculation number, 935439

Academic Year of 2020/2021

"When you are explaining a why you have to be in some framework that you will allow something to be true; otherwise you are perpetually asking why"

Richard Feynman

Abstract

A study about a new concept of a flow sensor is presented. The sensor configuration is based on the article by James P. Wissman, Kaushik Sampath, Simon E. Freeman and Charles A. Rohde *Capacitive Bio-Inspired Flow Sensing Cupula* by with the surface neuromast bio-inspired polydimethylsiloxane (PDMS) compliant cupula. Nevertheless, the sensor bending measuring system was changed to a double core optical fiber interferometric bending sensor (other than a capacitive system, prior utilized by James P. Wissman et al.) proposed by Qu H., Yan G. and Skorobogatiy M. in the article *Interferometric fiber-optic bending/nano-displacement sensor using plastic dual-core fiber* and adapted to the geometry proposed. This change is done with the intention to overcome the problems created by the liquid metal gallium alloy inside the sensor, such as the internal liquid metal flow in the sensor and the interaction of this fluid with the viscoelastic cupula, that affects the sensing capability. A series of 8 configurations of sensors were tested in 2D fluid-structure interaction simulations using COMSOL Multiphysics® software under laminar flow regime. The 8 sensors vary in height (1.5 mm and 3 mm), to minimize the flow distortion after the sensor, width (0.5 mm and 1 mm), to better fit the optical fibers inside the sensor, and material utilized in the optical fiber double core (fused silica glass and polycarbonate), with the goal of creating the most compliant sensor possible. Afterwards, the best performing sensor, chosen through a parametric analysis, is selected to be tested numerically in a 3D fluid-structure simulation. The results of the 2D simulations indicate that the polycarbonate optical fiber sensor with width of 0.5 mm and height of 3 mm gives the higher deflection in comparison with other 7 sensors, under all laminar regime flows, for Reynolds number from 0.01 to 2000. This sensor is chosen to be modeled in 3D to run the same kind of laminar flow fluid-structure

interaction analysis.

The final 3D modeled sensor shows promising numerical results for its sensing capability under two different interferometric techniques: the first one is the fringe detection method in which the threshold of detection is from $Re \approx 1200$ (corresponding in the proposed system to a mean flow velocity of 0.4 m/s) and the detection of the intensity of the interference signal technique, which gave the detection threshold of $Re \approx 15$ (corresponding in the proposed system to a mean flow velocity of $5 \cdot 10^{-3}$ m/s). Overall, the mechanical behavior of the sensor and the detection threshold shows that sensor configuration is viable, being needed yet laboratory testing and turbulent condition dynamic simulations.

Sommario

È qui presentato uno studio riguardo una nuova idea di sensore di flusso d'acqua. Il sensore proposto si basa sull'articolo di James P. Wissman, Kaushik Sampath, Simon E. Freeman and Charles A. Rohde *Capacitive Bio-Inspired Flow Sensing Cupula*, il quale presenta una cupola deformabile in PDMS, ispirata dai neuromasti superficiali dei pesci, rendendolo bio-ispirato. L'impianto che si occupa della misurazione della deformazione viene modificato da un sistema capacitivo a un sistema interferometrico costituito da due fibre ottiche, proposto da Qu H., Yan G. and Skorobogatiy M. nell'articolo *Interferometric fiber-optic bending/nano-displacement sensor using plastic dual-core fiber*, e che è stato adattato alla geometria consigliata. Una serie di otto impostazioni per il sensore è testata con simulazioni 2D d'interazione fluido-struttura (*fluid-structure interaction*) utilizzando il software COMSOL Multiphysics® software [1], sotto regime laminare di flusso d'acqua. Le otto impostazioni del sensore variano in altezza (1.5 mm e 3 mm) per minimizzare la distorsione del flusso una volta superato il sensore, spessore dei sensori (0.5 mm e 1 mm), per far adattare meglio le fibre ottiche presenti nel sensore, e materiale utilizzato per le fibre ottiche (vetro di silice fuso e policarbonato), con l'obiettivo di creare un sensore più flessibile. Dopodiché il sensore più performante, scelto tramite un'analisi parametrica, viene selezionato per essere testato numericamente in una simulazione 3D di struttura del fluido. I risultati delle simulazioni in 2D indicano che fibre ottiche in policarbonato di 0.5 mm di spessore e 3 mm di altezza danno maggior deflessione paragonate con quelle degli altri 7 sensori, tutti sotto regime laminare con numero di $0.01 < Re < 2000$. Questo sensore è scelto per essere modellizzato in 3D ed essere sottoposto allo stesso tipo di analisi d'interazione fluido-struttura sotto regime laminare.

Il sensore definitivo modellizzato in 3D mostra risultati numerici promet-

tenti per via delle sue capacità di rilevamento sotto due diverse tecniche interferometriche: la prima consiste nel metodo di rilevamento delle frange d'interferenza aventi come soglia minima $Re \approx 1200$ (corrispondente, nel sistema proposto, ad una velocità media del flusso di 0.4 m/s), mentre la seconda consiste nel rilevamento dell'intensità del segnale d'interferenza con $Re \approx 15$ (corrispondente nel sistema proposto ad una velocità media del flusso di $5 \cdot 10^{-3}$ m/s). In definitiva, il comportamento meccanico del sensore e la soglia di rilevamento mostrano che la configurazione del sensore è attuabile, nonostante necessiti ancora di test in laboratorio e di simulazioni dinamiche sotto regime di moto turbolento.

Acknowledgements

I would like to thank my supervisors, Professor Stefano Mariani from Politecnico di Milano and Professor Sabina Merlo from Università di Pavia, who always were attentive to my requests and were very gentle during our meetings. Beyond the academia, I would like to express my gratitude to my parents, Jorge Ferreira do Valle Neto and Solange Helena Vicentini, which were very supportive and without both of them my double degree at the Politecnico di Milano would not have been possible. I would like express my gratefulness to my uncles, José Eduardo Marques and Marilis Marques, who were very supportive during my studies.

To all my incredible friends, who always helped me through the course with academic, personal and Italian language matters during these two years away from home, I would like to express my gratitude. To name a few of these incredible persons I can mention: Viviane Grion Mielli, Júlia Kawamoto, Bruna Benevides, Júlia Freixedelo, Pedro Costa Braga, Jacopo Lavazza, Angela Giunto, Angelo Rivera, Francisco Atoche Perez, Francesca Cattaneo, Michela Capasso, Giulia Maria Ramella, Anna Danesin, Alessandro Verona, Marcello Bavaro, Angela Giannino, José Vidal Zobaran, Fabrizio Bueno Torres, between many others whose help was undeniable.

Contents

List of Figures

List of Tables

Chapter 1

Introduction

Mimicking nature to inspire new designs, materials, functionalities and behaviors, what is also as biomimicry [4], is widespread field of innovation and research in the academia, although it is still knowing its first days in the industry if compared to other areas [5]. Intelligent materials, sensors and actuators are already broadly explored as a research topic, with fields including bio-inspired color-changing sensing materials and bio-inspired shape-morphing actuating materials [6], shark drag-reducing scales in turbulent condition [7] and thunniform more efficient swimming capabilities of fish [8], among many others examples and applications.

A great variety of mechanisms to sense inputs from the environment are found in animals, such as, for light as an input, there is the retina of the human eye, that can convert the light input - electromagnetic radiation from the environment - into electrochemical impulses in the neurons through a complex system constituted by three layers: the first one the photoreceptors of light constituted of cones and rods cells, followed by the bipolar layer and the ganglion cell layer [9]; for the input as the strain of a joint, the chordotonal organ of some insects, like cockroaches, give information about the velocity, positioning and stretching of this joint through hundreds of individual sensory cells [10]; and, for the input as the flow and pressure of the water surrounding fish, hair-cells are sensible to it through a series of cilia connected to neurons, that when moved, create a electrochemical signal [11].

About this last detection mechanism, the method of flow detection for biosensors in nature and on the bio-inspired sensors are different: in the fish biosensor, as explained above, the motion can be detected by electrochemical responses [12–14], as for the bio-inspired systems the method can be based on a series of methods, that can include: piezoresistivity [**?**, 11, 15]; optic [16]; capacitive systems [2, 17]; and, piezoelectric [18, 19]. This latter piezoelectric kind of bio-mimetic sensor is based on a compliant polymer cupula structure, which is explored by Asadnia *et al* [19]. In their article, the sensor - which was based in the hair-cell biosensor, described by [11] - consisted of a piezoelectric motion-detection system, where the piezoelectric material used was the polyvinylidene fluoride (PVDF) in nanorod structures, attached to a rigid substrate in a specific configuration with polydimethylsiloxane (PDMS) supporting rods and a cupula made out of a hydrogel based on hyaluronic-acid (HA). This system had the detection limit for flow velocity of 8 μm/s, which is a result that overcome the capability of spiders and insects to sense flow, which is about 30 μm/s [20]. As for the article by James P. Wissman, Kaushik Sampath, Simon E. Freeman and Charles A. Rohde *Capacitive Bio-Inspired Flow Sensing Cupula* [2], which inspired the present thesis, they intended to create a compliant bio-inspired sensor that would mimic the sensitive capabilities of the surface neuromasts [21], structures present on the lateral line of fish, that help them to sense the water flow and orient aptly to it, a process called rheotaxis [12]. These lateral line neuromasts can be of two types: the surface neuromasts and the channel neuromasts, both of which consist in thousands of hair-cell like structures involved in a gelatinous cupula [16]. This lateral line neuromast can have the impressive capability of sensing waves with amplitudes down to 0,01 μm [22].

The way the autors from article [2] mimetized the surface neuromasts consists in a polydimethylsiloxane (PDMS) cupula with three separate internal cavities filled with liquid gallium alloys that served as capacitors in a capacitive system that would perceive the deformation of the cupula. The geometry of the sensor is depicted in Figure 1.1. This system uses a relation between the velocity of the incoming flow that deforms the compliant cupula, which induces a change in capacitance of the system, thus allowing the indirect measuring of the flow velocity through the capacitance. This system had a good overall performance, having a limit of detection of 60 mm/s in direct current of flow. Nonetheless, the combination of PDMS with a liquid metal capacitive system when exposed to a long duration test

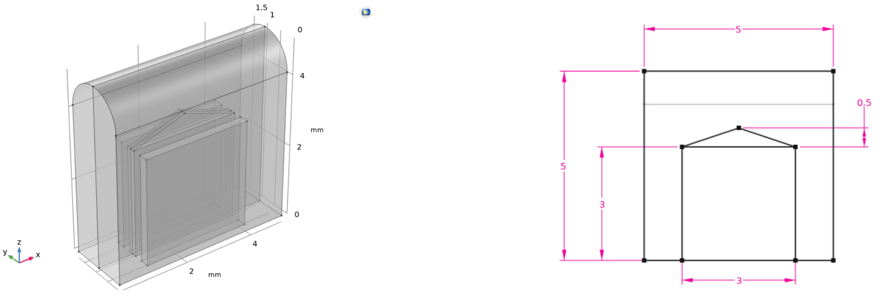

(a) Isometric view of the sensor used by [2]. The three internal cavities are filled with gallium alloys.

(b) Measures of the sensor by [2] in the xz plane. All measures are given in millimeters.

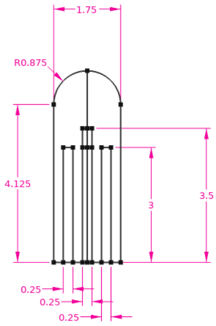

(c) Measures of the sensor by [2] in the yz plane. All measures are given in millimeters.

Figure 1.1: Geometries modeled with COMSOL Multiphysics ® software [1].

- 3,5 hours [2] - had a decrease in the the sensor precision of 15,4 %, due to the viscoelastic behavior of the PDMS together with the liquid metal behavior inside the sensor.

A distinct way of measuring the flow velocity - and even the velocity profile - is with optical techniques, which are are no novelty as bio-application sensors. For example, there are non invasive (a method that can measure the flow properties without any contact with it) methods such as optical feedback interferometry, in a study by [23], which has a good precision in the range of 16.8 mm/s to 168 mm/s and this technique, as shown by [24] can even reconstruct the velocity profile inside a micrometric duct.

An invasive optical method (a method that can measure the flow properties with some kind of contact with it) of detection of flow intensity and vortices was proposed by Klein A., Bleckmann H. in the article [16], in which the lateral line of fish was bio-mimitized with a series of PVC canals (squared cross-section with 4mm sides) and mimetic surface neuromasts structures. The biomimetic surface neuromasts are composed of a transparent silicon rod in contact with the flow that bends as the fluid passes through the channel, this transparent silicon rod has a laser light passing inside it that is captured at full intensity (with no flow in the channel, meaning that the sensor is perpendicular to the wall, at 90º with the wall of the channel) by a optical fiber on the opposite side of the channel, and, when it bends away from the 90º (fluid flow exists), the intensity of the light captured in the other side of the channel is changed, creating thus the detection mechanism. In a sense, the incorporation of a photonic inorganic method to a biomimicry sensor shows that under the right geometry and boundary conditions, such an approach can help to recreate organic organs, leading one step closer to real world applications of biomimicry sensors. Another invasive optical technique was used in [25], that can measure in real time the intravascular blood flow, which, according to the authors, would have a great impact in the decision making of a medical team, being another achievement for optical methods in bio-systems.

In between the various applications of optical techniques in the measure of flow profiles, intensity and real time monitoring it is possible to find that these techniques have a satisfactory application robustness in bio-systems.

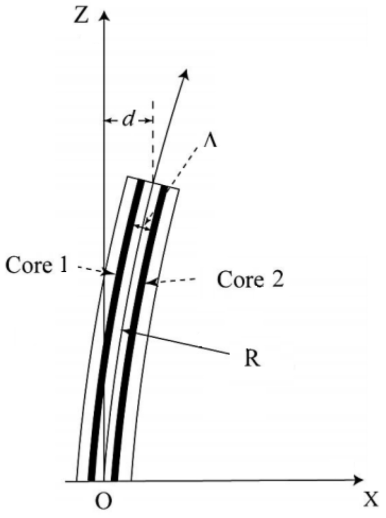

Figure 1.2: Figure adapted from [3]. Shows the geometry of the twin core optical fiber utilized in the proposed sensor.

Taking into account the latter considerations, this thesis proposes a new sensor configuration based on the model by [2] PDMS cupula sensor, changing the motion detection technique from a capacitive based one to an optical interferometry based one.

The new concept consists in utilizing a dual core optical fiber method based on the article by [3] inside the PDMS cupula. This system (Figure 1.2) is made out of two core optical fibers (designed by "Core 1" and "Core 2" in the figure) with a silver mirror layer on top which are involved by an external polymer cladding that is also present in between the two fibers, making the distance between the neutral axis of the fibers be of a distance Λ. In the Figure 1.2 is also possible to define the dislocation of the tip of the sensor d and the radius of curvature R when the sensor is bent. There are more complex setups which involves multiple optical fibers at its core, having the ability to detect deflections in two dimensions [26, 27]. That could be explored in our system in a next step of the study. Nevertheless, this study will focus on the numerical analysis of this novel kind of coupled compliant cupula and double core optical fiber interference system, to check its viability, proposing the geometry and the materials.

We propose four different geometries and two different optical fiber materials to couple the double core optical fiber interferometer, similar to [3] and the cupula present by [2] into a coupled interferometric microelectricalmechanical system (MEMS) flow sensor. Regarding the materials, we propose two different optical fibers for the dual-core interferometer: optical polycarbonate (PC), as used in [3], from the supplier [28], and optical fused silica glass Corning® 7940 [29]. Next, regarding the geometries, we propose 4 different geometries, that could fit the proposed sensor and we ran a parametric analysis to choose the sensor that would result in the higher phase difference in the interferometric system, thus having the best sensitivity. As the phase difference is directly proportional to the tip displacement, a series of stationary flow simulations in COMSOL Multiphysics ® [1] from $0.01 < Re < 1600$ are proposed to recognize which configuration result in the higher tip displacement, hence producing the higher phase difference in the interferometric system.

These geometries are proposed in a 2D framework in order to simulate with COMSOL Multiphysics ® [1] with a less computational demanding approach the mechanical response of the sensor to the incoming water flow

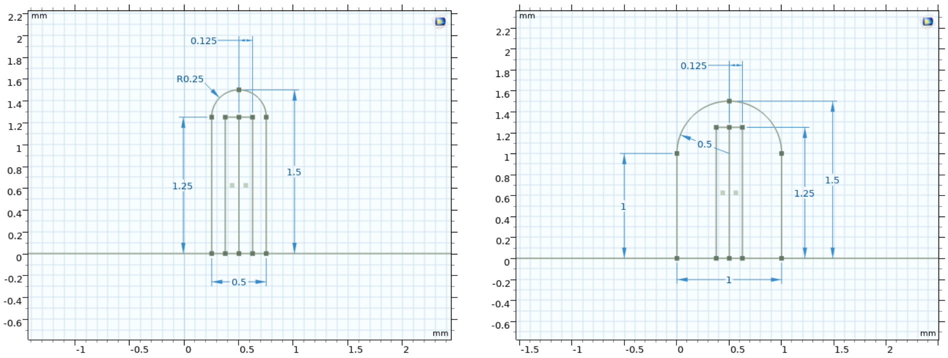

(a) Dimensions and geometry of the 2D sensor with 1.5 mm of height and 0.5 mm of width.

(b) Dimensions and geometry of the 2D sensor with 1.5 mm of height and 1 mm of width.

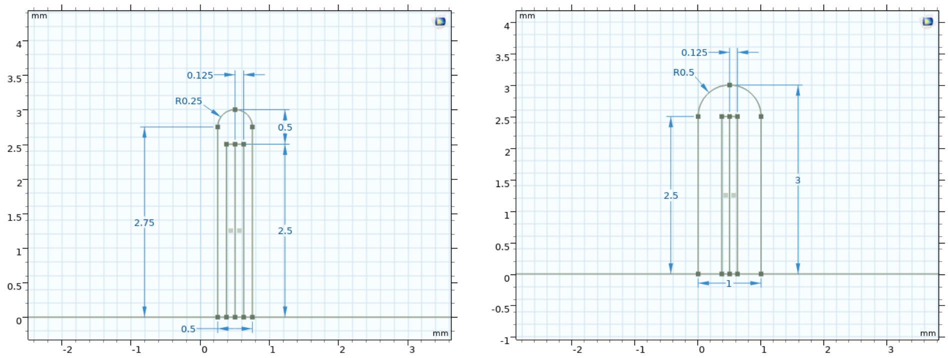

(c) Dimensions and geometry of the 2D sensor with 3 mm of height and 0.5 mm of width.

(d) Dimensions and geometry of the 2D sensor with 3 mm of height and 1 mm of width.

Figure 1.3: All 2D sensor geometries and dimensions, modeled with COMSOL Multiphysics ® software [1].

inside a millimetric channel. The variable parameters in the geometries are the height of the sensor and its width. To have a good cover of PDMS on top of the optical fiber we should have at least 0.5 mm of the PDMS thickness above the fiber on the 3 mm height sensor and, following that proportion, 0.25 mm of PDMS on top of the optical fiber in the 1.5 mm height sensor. All the dimensions are listed in figure 1.3 and summarized in the table 1.1. We consider the silver mirror to have negligible thickness, thus not being showed in figure 1.3 nor being considered in the table 1.1 dimensions.

Following the parametric analysis of the 2D geometries and materials, the best performing geometry and material will have the theoretical phase difference in the $0.01 < Re < 1600$ interval of water flow calculated, to check for the viability of the sensor in this flow interval. Later, in a 3D new proposed setup, which will be based in the best performing geometry

From figure 1.3	Width (mm)	Height of the sensor (mm)	Height of the Optical Fiber (mm)
(a)	0.5	1.5	1.25
(b)	1	1.5	1.25
(c)	0.5	3	2.5
(d)	1	3	2.5

Table 1.1: Table specifying the dimensions of the proposed 2D sensors.

and material from the 2D analysis, will be simulated under laminar flow conditions in COMSOL Multiphysics ® software [1], to check its viability and behavior.

1.1 Thesis structure

This thesis is presented with an abstract, a list of Contents, and then, it is structured in five main chapters and two appendices in the following way:

1. Chapter 1 is the introduction which will show a quick literature review of some methods utilized in the biomimicry of flow sensitive bio-sensors and a general framework of the work, presenting: the geometries and materials tested, the methods and simulations which were carried out in this work.

2. Chapter 2 includes the theoretical background for the simulations hereby presented. This will include the principles of the twin fiber optical interferometer, the governing equations for fluids and solids used in the framework that COMSOL Multiphysics ® uses for its simulations and a quick introduction of the finite element method for stationary systems.

3. In chapter 3, the results of the 2D proposed sensors fluid-structure interaction simulations will be presented and discussed. The boundary conditions, material properties, mesh settings and results will be described in detail. Then the parametric analysis of all geometries will be used in order to find the best candidate to have a higher phase difference, hence having more sensitivity to measure the water flow.

4. In chapter 4, the geometry of the 3D proposed sensor will be presented. Fluid-structure interaction simulations in a square cross section duct are performed in laminar flow to check the phase difference response of the sensor interferometer in the 3D proposed geometry.

5. Chapter 5 presents the conclusions of the study and proposes future developments for the present work.

6. In appendix A all the fluid velocity magnitude profiles for the 2D simulations are presented.

7. In appendix B all the fluid velocity magnitude profiles for the 3D simulation are presented.

This thesis also provides a list of figures and a list of tables after the table of contents, as well as an acknowledgments part prior to the table of contents.

Chapter 2

Theoretical Background

In this chapter the physical governing equations for the fluid and solid continuus mechanics will be described, aiming to give a overall view on the physics of the simulations run thorough this work. Next, a review on the finite element method will be presented. In the last section of this chapter, a overview on the calculation of phase difference between two optical fibers inside a core is presented, based on the articles by Qu et al. [3] and the one by Real Vallée and Denis Drolet [30].

In this work the hypothesis that the materials such as PDMS, polycarbonate, fused silica glass, and its composites in the sensor, have linear behavior under laminar flow regime, because the stresses applied are of small value due to low velocities of the flow and the small surface area in contact with the flow, thus they are modeled as isotropic Saint Vernant-Kirchhoff materials. These kind of linear mechanics only require the Young Modulus and the Poisson's ratio to be fully described, as it will be showed in this chapter.

All equations shown in this chapter are written in the index notation (or Einstein notation) for simplicity and to avoid heavy notation use.

2.1 Fluid Governing Equations

As the fluid is a mass conserving continuum medium, it must respect the continuity principle, given by:

$$\left(\frac{\partial}{\partial t}\right)\rho + \partial_i(\rho v_i) = 0, \tag{2.1}$$

where ρ is the density field of the fluid, v_i is the velocity vectorial field and t denotes time.

As for the moment transport inside a fluid, the general balance of momentum can be written as,

$$\rho\left[\left(\frac{\partial}{\partial t}\right)v_i + \partial_j(v_j v_i)\right] = \rho b_i + \partial_i \sigma_{ij}, \tag{2.2}$$

where b_i are the external forces applied to the fluid and the σ_{ij} is the tensor of stresses. In the fluid it can be written as,

$$\sigma_{ij} = -p(\rho)\delta_{ij} + \left[\eta_B(\rho) - \frac{2}{3}\eta(\rho)\right](\partial_k v_k)\delta_{ij} + \eta(\partial_i v_j + \partial_j v_i), \tag{2.3}$$

in which η is the shear viscosity, η_B is the bulk viscosity, δ_{ij} denotes the Kronecker delta and $p(\rho)$ the pressure that depends on the density. These two equations can be combined to give the Navier-Stokes equations [31],

$$\rho\left[\left(\frac{\partial}{\partial t}\right)v_i + \partial_j(v_j v_i)\right] = -\partial_i p + \partial_i\left[(-\eta_B + \frac{2}{3}\eta)\partial_k v_k\right] + 2\partial_i(\eta\partial_k v_k) + \rho b_i \tag{2.4}$$

2.2 Solid Governing Equations

To describe the mechanical behavior of a solid, from the continuum mechanics point of view, the conservation of four main quantities need to be achieved: the mass conservation (2.1), the momentum conservation (2.2), the angular momentum conservation and the conservation of energy [32]. The latter two can be written as, respectively,

$$\sigma_{ij} = \sigma_{ji}, \tag{2.5}$$

$$\sigma_{ij}d_{ij} + \rho r - \partial_i q_i = \rho\left[\left(\frac{\partial}{\partial t}\right)u_i + v_i\partial_i u_j\right], \tag{2.6}$$

where d_{ij} will be rate of deformation tensor with the unit of $[\frac{1}{s}]$, r will be a heat source with $[\frac{W}{kg}]$, ρ in the density with $[\frac{kg}{m^3}]$, q_i is the spatial heat flux vector with the units of $[\frac{W}{m^2}]$, u_i is the displacement vector $[m]$ and v_i is the velocity vector $[\frac{m}{s}]$. Therefore, both sides of the equation will have the units of energy flux per volume $[\frac{W}{m^3}]$.

Combining these field equations for continuum mechanics with a constitutive mode it is possible to model the mechanical behaviour of a material. In the case of this work, the linear elasticity for a Kirchhoff material will be used and described.

2.2.1 Green Strain Tensor (E)

The Green strain tensor is defined as the squared infinitesimal deformation on the current configuration minus the squared length of the initial configuration [32], as follows,

$$dx_i dx_i - dX_i dX_i = 2dX_i E_{ij} dX_j, \tag{2.7}$$

where dx_i is a vector which denotes the deformed system and dX_i is the vector that describes the original state of the material. On the right side of the equation the E_{ij} represents the Green strain tensor. This tensor can also be expressed with the spatial derivatives of the displacement vectors, which is the form used by the COMSOL Multiphysics® software [1]. This last form is,

$$E_{ij} = \frac{1}{2}\left(\frac{\partial u_i}{\partial X_j} + \frac{\partial u_j}{\partial X_i} + \frac{\partial u_k}{\partial X_i}\frac{\partial u_k}{\partial X_j}\right), \tag{2.8}$$

being u_i the displacement vector. An important relation occurs between the Green strain tensor with the rate of deformation tensor F_{ij}, which is described analytically as,

$$dx_i = F_{ij} dX_j. \tag{2.9}$$

This relation takes place when the left part of equation (2.7) is substituted by the rate of deformation tensor definition (2.9), resulting in the following,

$$dx_i dx_i - dX_i dX_i = 2dX_i E_{ij} dX_j, \tag{2.10}$$

$$dX_j (F_{ji})^T F_{ik} dX_k - dX_j \delta_{kj} dX_k = 2dX_j E_{jk} dX_k, \tag{2.11}$$

$$dX_j \left((F_{ji})^T F_{ik} - \delta_{jk} - 2E_{jk}\right) dX_k = 0, \tag{2.12}$$

then, as this last expression should work for any given dX, the final relation between these tensor is achieved:

$$E_{jk} = \frac{1}{2}\left((F_{ji})^T F_{ik} - \delta_{jk}\right). \tag{2.13}$$

2.2.2 Second Piola-Kirchhoff Stress Tensor (PK2)

A convenient way to describe the Second Piola-Kirchhoff stress tensor is by first introducing the Cauchy Stress tensor (σ_{ij}), which describes the stresses applied on an infinitesimal surface Γ of the domain $\Omega \subset \mathbb{R}^3$. Its formulation is,

$$n_i \sigma_{ij} d\Gamma = t_j d\Gamma, \tag{2.14}$$

where n_i is the normal vector to the infinitesimal surface area $d\Gamma$ and t_j is the traction vector acting on the infinitesimal surface $d\Gamma$. All the terms in the Cauchy tensor are placed in the present configuration. With the definition of the Cauchy Stress tensor, an elegant form of the PK2 tensor (S) can be written, which takes into account the rate of deformation tensor (F), its determinant (J) and the Cauchy tensor, as follows,

$$S_{ij} = J(F_{ik})^T \sigma_{kl} F_{lj}. \tag{2.15}$$

2.2.3 Saint Vernant-Kirchhoff Material

The Saint Vernant-Kirchhoff material constitutive model for linear elastic behavior utilizes the Green strain tensor (2.13) and the PK2 tensor (2.15) with a fourth-order tensor C_{ijkl} which describes all the possible elastic constants needed for the anysotropic response of the material. The major formulation of the constitutive model is,

$$S_{ij} = C_{ijkl} E_{kl}. \tag{2.16}$$

Due to major and minor symmetries in the system the 81 elements fourth-order tensor C_{ijkl}, can be fully described by just 21 independent constants. These latter constants, know as the *elastic moduli* of the material, can be further condensed if the material has a symmetric response to stresses. As do the isotropic materials, that have the same elastic response for stresses applied in any direction. Thus, this material has new symmetries that can simplify the *elastic moduli* tensor.

Using these symmetry relations combined with two materials mechanical properties: the Young Modulus E and the Poisson's Ratio ν, it is possible to describe fully the mechanical behavior of a isotropic linear elastic materials. To further simplify the description, the Lamé constants (λ, μ) are introduced, these constants are often used for elastic theory [33] and are written based on the Young Modulus and the Poisson's ratio as [32, 33],

$$\mu = \frac{E}{2(1+\nu)}, \tag{2.17}$$

$$\lambda = \frac{E\nu}{(1+\nu)(1-2\nu)}. \tag{2.18}$$

With the Lamé constants it is possible to write the *elastic moduli* tensor C_{ijkl} for isotropic elastic materials as the expression [32],

$$C_{ijkl} = \lambda\delta_{ij}\delta_{kl} + \mu(\delta_{ij}\delta_{kl} + \delta_{ij}\delta_{kl}), \tag{2.19}$$

where the δ_{ij} denotes the Kronocker Delta and the product between $\delta_{ij}\delta_{kl}$ denotes a external product (notice that the index do not permit a contraction), creating the identity fourth-order tensor.

The PK2 tensor can also be described in this reduced form for isotropic elastic materials, which would be [32]:

$$S_{ij} = \lambda E_{kk}\delta_{ij} + 2\mu E_{ij}, \tag{2.20}$$

where E_{kk} denotes the Einstein convention for the trace of the tensor E_{ij}.

2.3 Finite Element Method

The continuum mechanics partial differential equations (2.1, 2.2, 2.5, 2.6) cannot be solved analytically with ease, thus requiring numerical methods to provide results for different geometries and configurations [34]. The finite element method is the numerical method applied to major part of the mechanical analysis softwares, which includes the software used in the present work, COMSOL Multiphysics® [1].

This method will discretize the continuum domain into a grid of the points, the so-called nodes, by transforming the displacement field $u_i(X_j)$ [1] to a $u_i^\alpha(X_j^\alpha)$, in which α denotes the node index, for a α-node system. For computational purposes $u_i^\alpha(X_j^\alpha)$ can be written as a column matrix [31],

$$u_i^\alpha(X_j^\alpha) = \begin{bmatrix} u_i^1 \\ u_i^2 \\ \vdots \\ u_i^{\text{n-node}} \end{bmatrix} = \begin{bmatrix} u_1^1 \\ u_2^1 \\ u_3^1 \\ \vdots \\ u_1^{\text{n-node}} \\ u_2^{\text{n-node}} \\ u_3^{\text{n-node}} \end{bmatrix}. \tag{2.21}$$

This discrete displacement field still need to be interpolated to form a continuous differentiable and integrable function. For this reason the so-called shape-function S is applied to the nodes defining a new interpolated displacement field $\tilde{u}_i$. This function S must respect the displacement of each node alone, thus being required the Kronecker delta along the shape-function. The new approximated displacement field can be summarized as [31],

---

[1] Here the indexes i and j denote the index convention for a first order tensor, or a vector, being the vectorial function u_i dependent on the vector X_j (the original undeformed system coordinate system, as seen in subsection 2.2.1), where the indexes go from 1 to 3. For the orthonormal base $e_i = (e_x, e_y, e_z)$, $u_1 // \vec{e}_x$, $u_2 // \vec{e}_y$ and $u_3 // \vec{e}_z$.

$$u_i(X_j) \approx \tilde{u}_i(X_j) = S_{i\alpha}u_\alpha = \begin{bmatrix} S^1 & 0 & 0 & & S^{n-node} & 0 & 0 \\ 0 & S^1 & 0 & \dots & 0 & S^{n-node} & 0 \\ 0 & 0 & S^1 & & 0 & 0 & S^{n-node} \end{bmatrix} \begin{bmatrix} u_1^1 \\ u_2^1 \\ u_3^1 \\ \vdots \\ u_1^{\text{n-node}} \\ u_2^{\text{n-node}} \\ u_3^{\text{n-node}} \end{bmatrix}, \tag{2.22}$$

where, the node approximated by the $\tilde{u_i}$ function must be the the original node only, thus introducing the Kronecker delta,

$$u_i^\alpha = \tilde{u}_i(X_j^\alpha) = \sum_{\beta=1}^{n-node} S^\beta(X_j^\alpha)u_i^\beta = \sum_{\beta=1}^{n-node} \delta_{\alpha\beta}u_i^\beta. \tag{2.23}$$

Next, having the definition of the discrete displacement field, the deformation gradient (eq. (2.9)) can be rewritten as a function of it, as follows,

$$F_{ij} \approx \tilde{F}_{ij} = \delta_{ij} + \frac{\partial \tilde{u}_i}{\partial X_j} = \delta_{ij} + \sum_{\alpha=1}^{n-node} \frac{\partial S^\alpha}{\partial X_j} u_i^\alpha. \tag{2.24}$$

Now, it is possible to write the elastic strain energy (**??**) w as a function of the gradient of deformation $\tilde{F}_{ij}$ because the Green strain is a function of the gradient of deformation as $E_{ij}(\tilde{F}_{ij})$ and the elastic strain can be written as a function of the Green strain. Therefore, $w(E_{ij}(\tilde{F}_{ij})) = w(\tilde{F}_{ij})[\frac{J}{m^3}]$, which integrated on the volume of the original domain Ω_0 and subtracted by body forces $b_i[\frac{J}{m^2}]$ applied at the initial surface $\partial\Omega_0$ integrated on this surface will result in the total potential energy of the system U. This total energy is a functional of the displacement field u_α, thus the Euler-Lagrange equation is applicable to find the geodesic function u_α that minimizes the energy of the functional.

The total potential energy functional $U[u_\alpha]$ can be expressed,

$$U[u_\alpha] = \iiint_{\Omega_0} w(\tilde{F}_{ij}(u_\alpha))dV_0 - \iint_{\partial\Omega_0} b_i S_{i\alpha} u_\alpha dA_0, \tag{2.25}$$

where V_0 denotes the initial value of the volume and A_0 the initial surface area of the Ω domain.

The next step will be to minimize of the total potential energy of the system. This is done in order to find the equilibrium state of a stationary mechanical system, whose energy is described by the equation (2.25). Mathematically, the functional derivative of $U[u_\alpha]$ with relation to u_α, when equaled to zero will give the equilibrium state of the mechanical system. This idea is be summarized as,

$$-\frac{\delta U[u_\alpha]}{\delta u_\alpha} = 0, \tag{2.26}$$

which is equivalent, in physical terms, to the $F_i = -\partial_i U$ (where F is a force vector and U is a generic potential field), where a force can be derived from the potential energy field, resulting in a force, that in this work will be a vector named $f_{i,\alpha}$, explaining why the expression (2.26) takes the negative sign.

Next, taking the derivative of (2.25),

$$f_{i,\alpha}(u_\alpha) = -\frac{\delta U[u_\alpha]}{\delta u_\alpha} = -\iiint_{\Omega_0} \frac{\partial w}{\partial \tilde{F}_{ij}} \frac{\partial \tilde{F}_{ij}}{\partial u_\alpha} dV_0 + \iint_{\partial\Omega_0} b_i S_{i\alpha} dA_0, \tag{2.27}$$

where the derivative of the elastic strain energy is splitted into two derivatives by the chain rule, expliciting the derivative of the gradient of deformation tensor by the displacement field, which by itself is equal to the first derivative of the PK2 tensor with respect to the deformed configuration X_i [31],

$$\frac{\partial w}{\partial \tilde{F}_{ij}} = \frac{\partial S_{i\alpha}}{\partial X_j}. \tag{2.28}$$

To conclude this derivation, presented more formally by [31], the final form of the minimization of energy with the PK2 tensor is,

$$f_{i,\alpha}(u_\alpha) = -\iiint_{\Omega_0} P_{ij}(\tilde{F}_{ij}(u_\alpha)) \frac{\partial S_{i\alpha}}{\partial X_j} dV_0 + \iint_{\partial\Omega_0} b_i S_{i\alpha} dA_0, \tag{2.29}$$

where,

$$P_{ij}(\tilde{F}_{ij}(u_\alpha)) = \frac{\partial w}{\partial \tilde{F}_{ij}}. \tag{2.30}$$

To make the functional derivative (2.26) be equal to zero, it must be evaluated in a displacement field $u_{\alpha,0}$ that will be the solution to the equilibrium state of the mechanical system. To do so, numerical methods to find the zero of the function $f_{i,\alpha}(u_\alpha)$ (out-of-balance forces must be null to have the equilibrium system) are required, as the P_{ij} function is nonlinear and has to be solved iteratively. A number of numerical methods can be used to solve this type of problem, between then there is the Newton-Raphson method, the line search method and others. The topic of numerical methods to find roots of functions won't be further discussed as it is not on the scope of this work.

2.4 Double Core Optical Fiber Interferometer Principles

The double core optical fiber system relays on the interference pattern created by a monochromatic laser beam split into two phase coherent beams that are guided by each optical fiber and reflected at the top silver mirror and, then, reunited, giving the interference pattern. This interference pattern is only created if there is a phase difference between the split beams when they return to the base of the optical fiber (given by coordinate O in the Z axis in figure 1.2), otherwise a constructive interference pattern would be observed.

The phase difference created due to the change in optical path experienced by each fiber, $\Delta\phi_1 = k\Delta L$, being $\Delta\phi_1$ the phase delay, k the wavenumber (defined by $k = \frac{2\pi}{\lambda}$, where λ is the wavelength), and ΔL the change in the path or length of the fiber, that occurs when the whole system is bent. This path difference ΔL can be translated to the Green Strain tensor in the YY direction (direction parallel to the neutral axis of the fiber), as shown next,

$$\Delta\phi_1 = kn_0\Delta L = kn_0E_{22}L = kn_0E_{YY}L, \tag{2.31}$$

where n_0 is the refractive index of the material and L is the length of the optical fiber [30]. Furthermore, there is the photoelastic effect which must be taken into account, in which the refractive index is changed with the strain applied to a material. The general equation of photoelasticity can be written as [30],

$$\delta n_i = -\frac{n_0^3}{2} p_{ij} \epsilon_j, \tag{2.32}$$

where δn_i is the change in refractive index of a fiber, represented as a vector by the i subscript, p_{ij} is the photoelastic tensor for a isotropic material (in this case polycarbonate) and ϵ_i is the strain in Voigt notation, with the subscript i varying from 1 to 3, just XX, YY and ZZ, directions. For the two-core optical bending sensor, this tensorial equation can be simplified as a difference between the refractive index change in both fibers [3],

$$\Delta n = -\frac{Cn^3 \Lambda}{2R}, \tag{2.33}$$

in which Δn denotes the difference in the refractive index between the two fibers, C denotes the photoelastic constant for the problem (a combination of components of the tensor p_{ij}), R is the radius of curvature of the fibers and Λ is the distance between the two optical cores.

Writing both contributions to the final phase difference, the final expression to the phase difference between the two cores of optical fibers ($\Delta\phi_1$ and $\Delta\phi_2$) can be approximated to [3],

$$\Delta\phi = \Delta\phi_1 - \Delta\phi_2 \approx 2kn_0 L[(\frac{\Delta n}{n_0}) + (\frac{\Delta L_1 - \Delta L_2}{L})], \tag{2.34}$$

being ΔL_1 and ΔL_2 the changes in length in the y direction for optical fibers 1 and 2, respectively (cores 1 and 2 in figure 1.2). If we want to use the Green strain directly in 2.34, it can be rewritten as,

$$\Delta\phi \approx 2kn_0 L[(\frac{\Delta n}{n_0}) + (E_{22}^1 - E_{22}^2)], \tag{2.35}$$

where the subscript in E_{22} denotes the direction YY and the super index the optical fiber. To further adapt the equation 2.35 to the variables present in this thesis, it would be interesting to calculate Δn bypassing the radius of curvature, utilizing just the Green strains. In order to so, the equation 2.32 can be directly used with the component of the photoelastic tensor p_{ij} being C, introduced in [3] for polycarbonate fibers. Thus, Δn would be,

$$\Delta n = (\delta n_i)_{fiber1} - (\delta n_i)_{fiber2} = -\frac{Cn^3}{2}(E_{22}^1 - E_{22}^2). \tag{2.36}$$

With these equations it is possible to calculate the theoretical phase difference of the twin optical fiber curvature sensor. To unify everything in one final equation, we have,

$$\Delta\phi \approx 2kn_0L(E_{22}^1 - E_{22}^2)\left[1 - \frac{Cn^2}{2}\right]. \tag{2.37}$$

Chapter 3

2D Geometries Sensor Simulations

In this chapter four geometries with two different materials for the optical fibers are numerically tested in a fluid-structure finite-element method analysis, utilizing COMSOL Multiphysics® [1], varying the height of the sensor and its width. The objective is to find the most compliant cupula with this pre-defined geometries and to analyze the way that would minimize the perturbation of the flow for microfluidic systems. The new geometries are proposed to include the bio-inspired cupula sensor from [2] with the interferometric double core optical fiber bending sensor proposed by [3] in a

3.1 Material properties and simulation parameters

The polydimethylsiloxane (PDMS) cupula utilized uses the same mechanical properties from [2] with some extra parameters added, such as the Poisson's Ratio of 0.495 [35], the density of, approximately, 970 kg/m^3 [36] and the Young Modulus of 750 kPa as used in the simulations by [2]. The same mechanical properties for the PDMS cupula are used in every simulation.

For the optical fiber component, two different materials were used: the optical polycarbonate (PC), as used in [3], from the supplier [28], and optical fused silica glass Corning® 7940 [29]. All their mechanical properties are summarized in the table 3.1.

Material	Density (kg/m^3)	Poisson's Ratio	Young Modulus (MPa)
PDMS	970	0.495	0.75
Fused Silica Glass	2201	0.179	72.1x10^3
Polycarbonate	1200	0.37	2.35x10^3

Table 3.1: Table with all utilized mechanical properties in the simulations, for each material.

Regarding the simulation parameters, COMSOL Multiphysics® [1] was the chosen finite element method software, as it can integrate different physics in the same analysis, such as with the fluid-structure interaction package, that was required to evaluate the strain in the optical fibers and the tip displacement with different water flux values hitting the sensor. The COMSOL Multiphysics® physics packages utilized were: Solid Mechanics with the option for linear elastic materials (also for PDMS which is exposed to small strain deformations), which uses the solid governing equations, found in section 2.2, and, as shown in chapter 2.2.3, just two material properties, the Young Modulus and the Poisson's Ratio, are able to describe the mechanical behavior of the material; the Laminar Flow (no turbulence was modeled in the present work) package which solves the fluid-governing equations, found in 2.1, in laminar regime, and finally the fluid-structure interaction package, which will calculate the final behavior of the sensor when hit by the water flow.

The channel utilized has the same cross section as the channel used by [2], a square cross section duct with 11.25 mm of height and 60 mm of length, show in figure 3.1. The sensor is put 20 mm away from the inlet of fluid (placed on the left), this way leaving 40 mm of duct before the outlet to analyze the flow behavior before the outlet. The inlet is set to permit a mass flow entry defined by the Reynolds number,

$$F = 2 \cdot H \cdot Re \cdot \eta, \tag{3.1}$$

where H stands for the height of the duct, Re stands for the Reynolds number and η stands for the dynamic viscosity of water at 25ºC. The outlet was set to the boundary condition of pressure equals to atmospheric pressure.

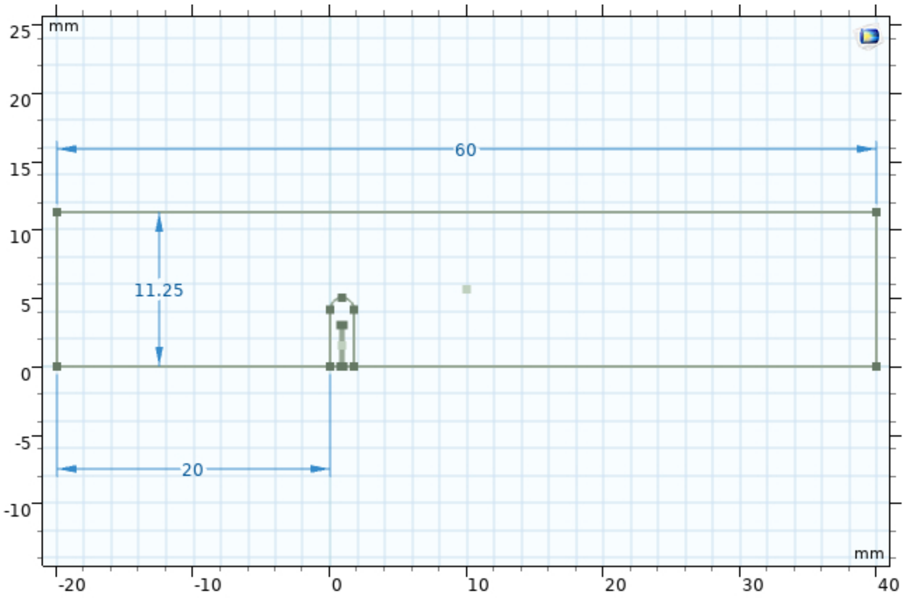

Figure 3.1: Diagram providing the dimensions (in millimeters) of the channel utilized in the fluid-structure interaction 2D simulations. Done with COMSOL Multiphysics® [1]

The laminar flow was taken to be the behavior of the flow inside the square cross-section until $Re = 2000$, as studied by [37]. To save computational efforts, the parametric analysis of the eight sensor configurations was set to occur in laminar flow from the low value of $Re = 0.01$ (mean flow velocity of $1.7976 \cdot 10^{-6}$ m/s), to be able to find the limit of detection of the sensor, until the limit of the laminar flow Reynolds number of $Re = 2000$ (mean flow velocity of 0.35953 m/s).

Regarding the mechanical contacts inside the sensor, both optical fibers are in contact, thus exerting a frictional force on each other. To model this contacts in COMSOL, assemblies were created between the internal parts of the sensor (PDMS cupula and the two independent optical fibers), and for what concerns the contact forces, they can be added in COMSOL Multiphysics® defining the friction coefficient of the optical fibers, glass-glass [**?**] and PC-PC [38], the values are reported in table 3.2.

Although the friction contact was set between the optical fibers, it was not added in the optical fiber-PDMS interface because this thesis does not propose the fabrication method of the sensor, being non realistic to imposed the pressure in the interface between the optical fiber and the cupula. Hence, this interface is set to be a adhesion interface with the gap between the fiber

Material	Friction Coeffient with itself
Fused Silica Glass	0.4
Polycarbonate	0.24

Table 3.2: Table containing the values of the coefficient of friction between the optical fibers inside the sensor.

and the cupula equals to zero.

Other general considerations that were made in the simulations and are worth mentioning are the fixed constrain boundary conditions (the basis is fixed, no movement is allowed) that were made in the basis of the sensor (both in the PDMS part and in the optical fiber part), as show in figure 3.2, that shows the basis of the sensor in blue, which is were the fixed constrains were applied. And, regarding the fluid dynamics boundary conditions, the no-slip condition applied on the walls of the sensor and of the channel to further simplify the simulation, taking into account that the damping created by the no-slip condition weakly diverges from the slip condition, as it was shown by [39], thus being a good approximation for the simulation at hand.

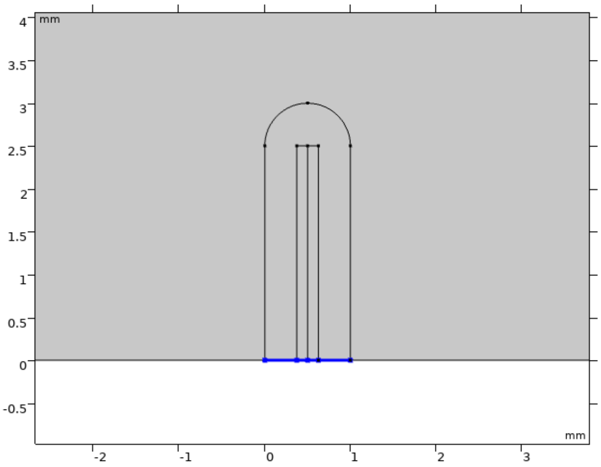

Figure 3.2: Diagram representing the fixed boundaries on the bottom of the sensor inside the microfluidic channel, with the fixed constrains in the bottom of the sensor in blue. The sensor represented here has 3 mm of height and 1 mm of width. Done in COMSOL Multiphysics® [1]

The mesh settings were the Physics-Controlled mesh from COMSOL

Multiphysics®, in which the software calculate the most suited free tetrahedral mesh based on the physics packages and multiphysics included in the problem, which in this case are the solid mechanics physics, laminar flow physics and fluid-structure interaction multiphysics package. These mesh settings have nine predefined mesh setups, that go from extremely coarse mesh to extremely fine mesh, from which was chosen the extra fine mesh, one preset before the extremely fine. The mesh for each one of the 4 geometries proposed is shown below, in figure 3.3.

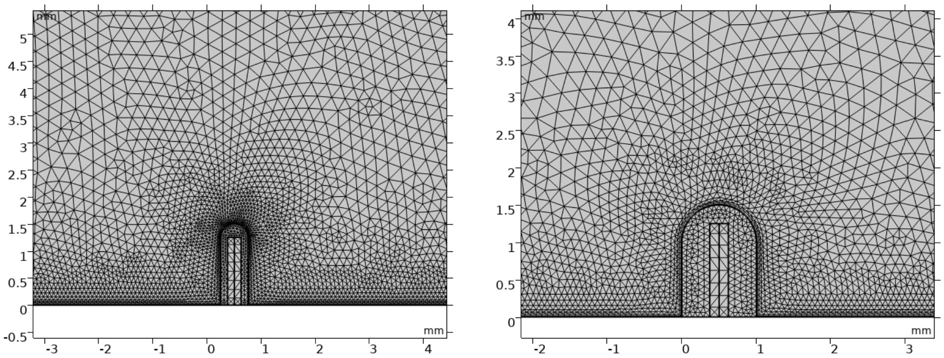

(a) Mesh settings for sensor with dimensions and geometry of the 2D sensor with 1.5 mm of height and 0.5 mm of width.

(b) Mesh settings for sensor with dimensions and geometry of the 2D sensor with 1.5 mm of height and 1 mm of width.

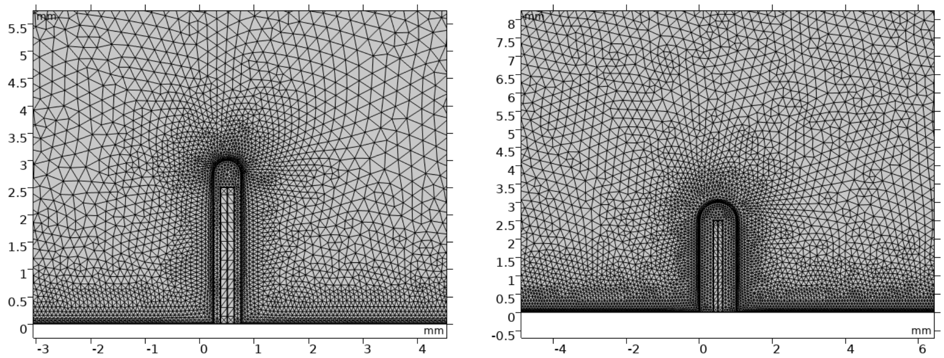

(c) Mesh settings for sensor with dimensions and geometry of the 2D sensor with 3 mm of height and 0.5 mm of width.

(d) Mesh settings for sensor with dimensions and geometry of the 2D sensor with 3 mm of height and 1 mm of width.

Figure 3.3: Free tetrahedral mesh for each one of the 4 geometries proposed, performed by auto-meshing presets included in COMSOL Multiphysics ® software [1].

3.2 Fluid-Structure Interaction Results and Discussion

In this section the results of the simulations of the four geometries proposed in the introduction (1) and in figure (1.3) and two materials for the optical fiber - what totalizes 8 different sensor configurations - will be presented and discussed. In order to discern the behavior of the various sensor geometries when exposed to water fluxes inside a microfluidic channel (the one presented in figure 3.1), a series of stationary simulations were performed.

To evaluate the behavior of the sensor at low flux velocities, 100 stationary simulations were performed for $0.01 < Re < 1$ (one hundred independent simulations, not increasing linearly the water flux with time) and to evaluate until the end of the laminar regime, 1000 simulations were performed from $1 < Re < 2000$. This simulations were not very time consuming as all 8800 simulations took nearly two days to compute, thanks to the 2D framework and the laminar regime package, which is much less time consuming than the turbulent flow packages.

The result aimed to be achieve is the tip displacement of the optical fibers (for each sensor configuration), which is directly proportional to the strain of this same fiber, as a function of the Reynolds number, and how this functions grows (first derivative of the tip displacement in respect to the Reynolds number). Some of the simulations presented convergence problems for Reynolds numbers close to 2000, which will be discussed. Nonetheless, the overall growth tendency of the non converging simulations curves is still observed.

The first results include the velocity profile around and after the proposed sensors, as shown in figure A.2 in appendix A. It can be observed that for Reynolds number equals to one, the laminar flow around every geometry of the sensor becomes unperturbed immediately after the sensor, creating a zone of high velocity on top of the sensor, but not perturbing the overall development of the flow after the sensor. This result is observed in the sensor with both optical fiber materials.

When the Reynolds number gets to higher values, the velocity magnitude of the flow shows a significant perturbation for the sensors with height of 3 mm, not returning to the original flow profile before the end of the channel, as observed in figures in A.1 in appendix A. This simulations with the 3 mm sensors did not converge for values beyond $Re = 413$ in the case of the fused silica glass with 0.5 mm cupula width, and, from $Re = 1551$ in the case of the case of the fused silica glass with 1 mm cupula width. The sensors with 1.5 mm cupula height showed a small distortion in the flow directly after the sensor, at $Re = 1999$.

In a microfluidic device working in laminar condition, such as the acoustic separation of particles suspended in a solution, the laminar regime is of the utmost importance, for being one of the working principles of the technique [40, 41]. From this point of view, the sensors with 1,5 mm would be the most suited to prevent the flow perturbation even at the limits of the laminar regime ($Re = 2000$).

Next, the displacement magnitude of the sensors was analyzed for $0.01 < Re < 1$ and then for $1 < Re < 2000$ in order to obtain the higher displacement of the optical fiber sensor tip. An overall view of the displacement of the hole sensor when hit by the stationary water flow with $Re = 1$ is reported in figure 3.4 and with the maximum achieved Reynolds number in the 3.5.

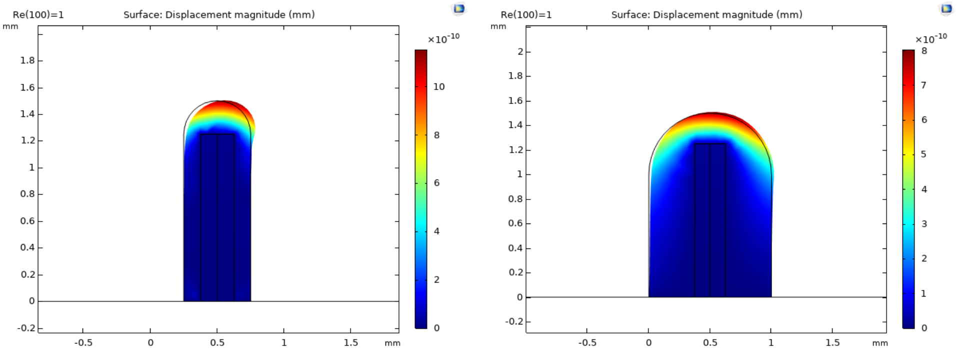

(a) PC twin core sensor with 1.5 mm of height and 0.5 mm of width.

(b) Fused silica glass twin core sensor with 1.5 mm of height and 1 mm of width.

Figure 3.4: Sensor displacement magnitude, for fused silica glass optical fiber twin core sensor 3.4a, 3.4b, 3.4c, 3.4d, and for polycarbonate optical fiber twin core sensor 3.4e, 3.4f, 3.4g, 3.4h, under laminar water flow at $Re = 1$. *Simulations and graphics done in COMSOL Multiphysics ® software [1].*

From figures 3.4 and 3.5 it is possible to see, from the order of magnitude of the displacements, that the polycarbonate optical fiber two core sensor is more complaint to a stationary water flow than the fused silica two core optical fiber sensor. From the orders of magnitude, it is observed that

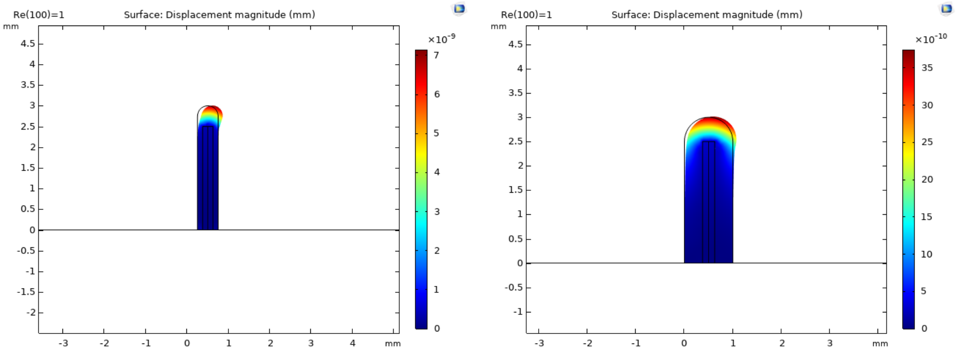

(c) Fused silica glass twin core sensor with 3 mm of height and 0.5 mm of width.

(d) Fused silica glass twin core sensor with 3 mm of height and 1 mm of width.

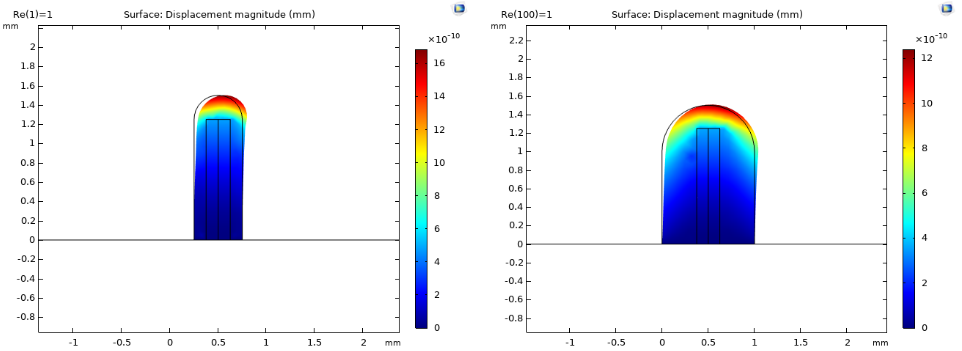

(e) PC twin core sensor with 1.5 mm of height and 0.5 mm of width.

(f) PC twin core sensor with 1.5 mm of height and 1 mm of width.

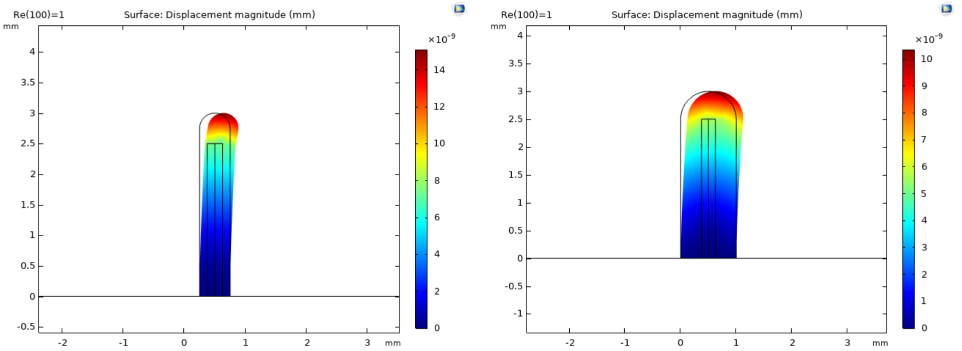

(g) PC twin core sensor with 3 mm of height and 0.5 mm of width.

(h) PC twin core sensor with 3 mm of height and 1 mm of width.

Figure 3.4: Sensor displacement magnitude, for fused silica glass optical fiber twin core sensor 3.4a, 3.4b, 3.4c, 3.4d, and for polycarbonate optical fiber twin core sensor 3.4e, 3.4f, 3.4g, 3.4h, under laminar water flow at $Re = 1$. *Simulations and graphics done in COMSOL Multiphysics ® software [1].*

when $Re = 1$, the displacements are in between $10^{-11}m < \delta < 10^{-13}m$ (being δ the displacement magnitude), which are smaller than the Bohr Radius ($\approx 0.53\mathring{A}$), therefore having no physical meaning for the analyzed macroscopic system. Passing to higher mean velocity flows, the displacement magnitude arrives to $\delta \approx 10^{-8}m$, which is a low displacement, but in the order of magnitude of the resolution of the interferometer two core optical fiber sensor proposed by [3].

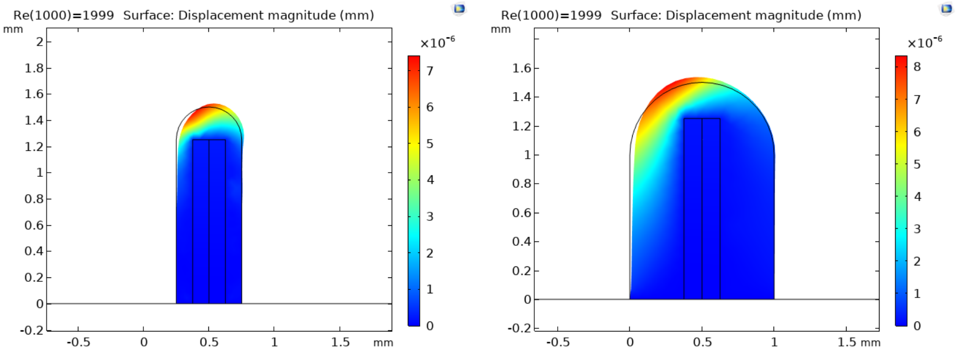

(a) Fused silica glass twin core sensor with 1.5 mm of height and 0.5 mm of width.

(b) Fused silica glass twin core sensor with 1.5 mm of height and 1 mm of width.

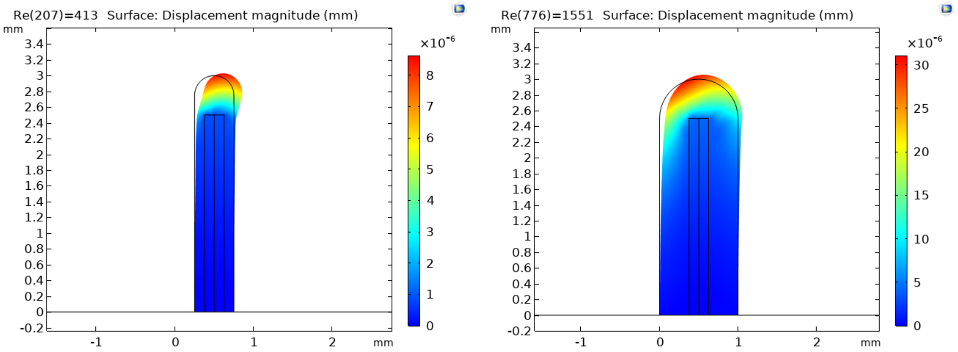

(c) Fused silica glass twin core sensor with 3 mm of height and 0.5 mm of width.

(d) Fused silica glass twin core sensor with 3 mm of height and 1 mm of width.

Figure 3.5: Sensor displacement magnitude, for fused silica glass optical fiber twin core sensor 3.5a, 3.5b, 3.5c, 3.5d, and for polycarbonate optical fiber twin core sensor 3.5e, 3.5f, 3.5g, 3.5h, under laminar water flow at the highest achieved Reynolds number. Simulations and graphics done in COMSOL Multiphysics ® software [1].

To summarize the data obtained, the graphic 3.6 chart the tip displacement of each optical fiber for each one of the eight sensors, against the Reynolds number of the water flow, in the x-axis (direction of the flow, defined in Figure 1.2). This first graphic comprehend the small deformation limit $0.01 < Re < 1$, with the units in millimeters. In this graphic a linear

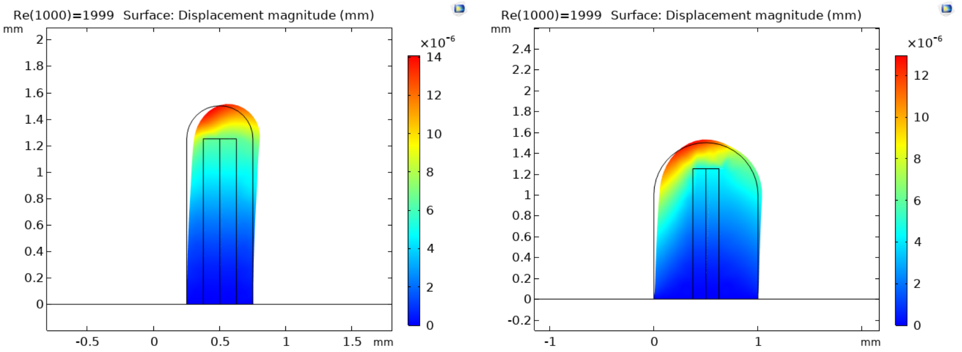

(e) PC twin core sensor with 1.5 mm of height and 0.5 mm of width. *(f) PC twin core sensor with 1.5 mm of height and 1 mm of width.*

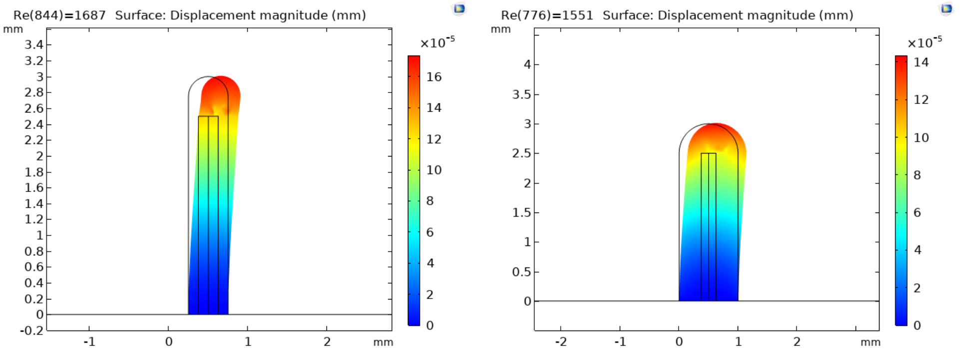

(g) PC twin core sensor with 3 mm of height and 0.5 mm of width. *(h) PC twin core sensor with 3 mm of height and 1 mm of width.*

Figure 3.5: Sensor displacement magnitude, for fused silica glass optical fiber twin core sensor 3.5a, 3.5b, 3.5c, 3.5d, and for polycarbonate optical fiber twin core sensor 3.5e, 3.5f, 3.5g, 3.5h, under laminar water flow at the highest achieved Reynolds number. Simulations and graphics done in COMSOL Multiphysics ® software [1].

increase of the tip displacement in the x-axis is observed with the increase of the Reynolds number.

As for the data that comprehend the simulations between $Re = 1$ and the maximum calculated Reynolds number for each configuration, the graphic 3.7 includes the tip displacement for each optical fiber inside the sensor plotted against the Reynolds number. In this graphic a quadratic behavior of the tip displacement is starting to show its form, as expect from the theoretical calculation from [2]. Yet, from graphic 3.7, the geometry and material that showed the most promising results regarding the maximization of the tip displacement, was the 0.5 mm width and 3 mm height sensor with polycarbonate optical fibers in its core, which reached $\delta \approx 10^{-7} m$ at $Re \approx 1670$. The second most compliant sensor - on the basis of the bending stiffness -

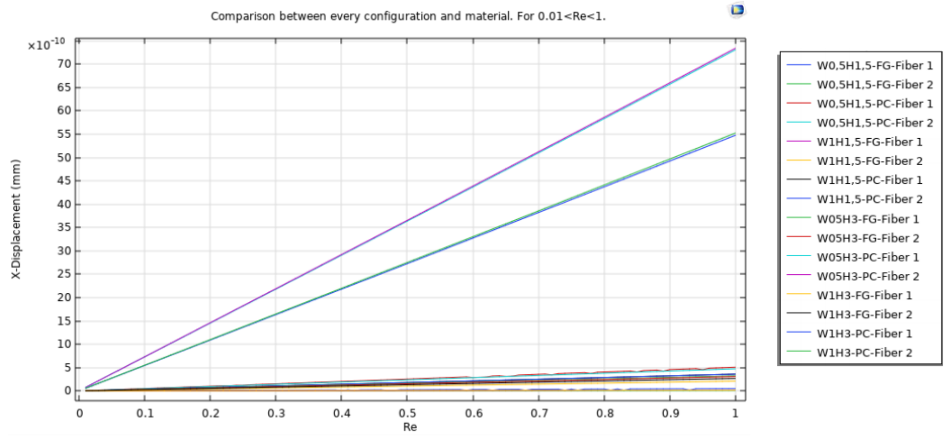

Figure 3.6: Plot for the tip displacement of each optical fiber tip for each sensor configuration, plotted against the Reynolds number. The legend on the right shows the nomenclature of the sensor width (W) in millimeters, height (H) in millimeters, fused silica glass (FG) and polycarbonate (PC). Obs: 05 stands for 0.5 mm in the nomenclature, as well as 1,5 stands for 1.5 mm.

was the 1 mm width and 3 mm height sensor with polycarbonate optical fibers in its core, which indicates that in our comparison, the polycarbonate shows better performance as a complaint sensor. The sensors with fused silica glass optical fibers in its cores showed a low deformation with the flow increase. This can be explained for the higher Young Modulus of the glass fiber, almost thirty times higher than the polycarbonate.

To analyze numerically this supposition a parametric analysis is performed in the next section.

3.3 Parametric Analysis

The methodology utilized to choose the best combination of material for the optical fiber and geometry of the sensor is a parametric analysis where the amount of tip displacement (in the x-axis) of the sensor related with the increase in the mean velocity of the incoming flow. This analysis was performed in the linear deformation range, for low Reynolds number values, taking the linear coefficient of the linear regression equation of each simulation, which has the units of mm. The figure 3.8 shows four graphics, two for polycarbonate core sensor and two for the silica glass core sensor, in which for a fixed width, the height is varied.

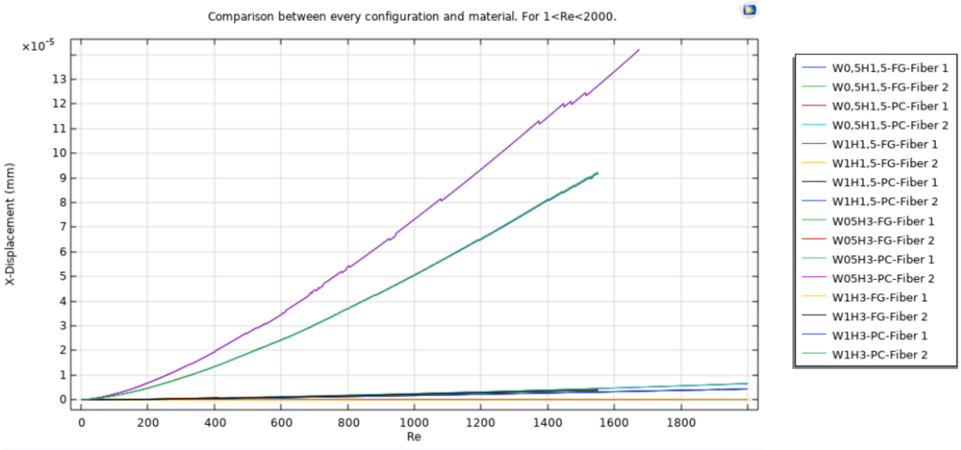

Figure 3.7: Plot for the tip displacement of each optical fiber tip for each sensor configuration, plotted against the Reynolds number. The legend on the right shows the nomenclature of the sensor width (W) in millimeters, height (H) in millimeters, fused silica glass (FG) and polycarbonate (PC). Obs: 05 stands for 0.5 mm in the nomenclature, as well as 1,5 stands for 1.5 mm.

width\height (mm)	1.5	3
0.5	$5 \cdot 10^{-6}$	$7 \cdot 10^{-5}$
1	$4 \cdot 10^{-6}$	$5 \cdot 10^{-5}$

Table 3.3: Table that organizes the linear coefficients of the the parametric analysis performed on figure 3.8 for polycarbonate optical fiber cores. Each column gives one height of the sensor and each row one width, creating all the four configuration possible. The number inside represents the linear coefficient of each curve, in units [mm].

width\height (mm)	1.5	3
0.5	$4 \cdot 10^{-7}$	$3 \cdot 10^{-6}$
1	$2 \cdot 10^{-7}$	$2 \cdot 10^{-6}$

Table 3.4: Table that organizes the linear coefficients of the the parametric analysis performed on figure 3.8 for fused silica glass optical fiber cores. Each column gives one height of the sensor and each row one width, creating all the four configuration possible. The number inside represents the linear coefficient of each curve, in units [mm].

The linear coefficients are placed in tables 3.3, for polycarbonate optical fiber cores, and 3.4, for fused silica optical fiber cores, to help to visualize the results.

From both tables, it is possible to arrive to the same conclusion that the 3 mm height and 0.5 mm thick polycarbonate optical core sensor is the sensor that presents the higher tip-displacement by velocity change ratio,

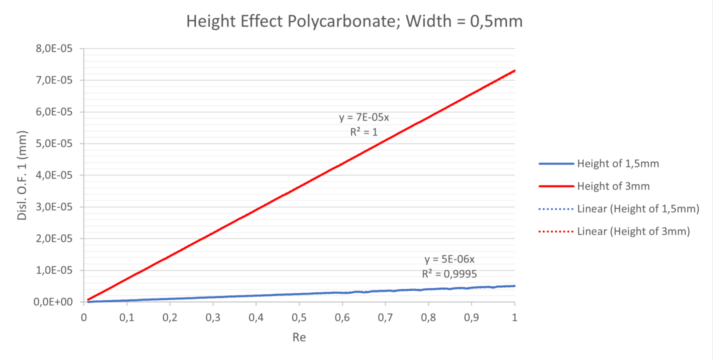

(a) Fixed width of 0.5 mm with 1.5 mm and 3 mm varying height for polycarbonate optical fiber core sensor.

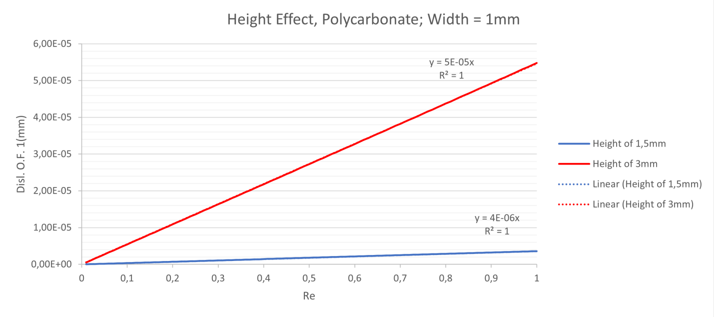

(b) Fixed width of 1 mm with 1.5 mm and 3 mm varying height for polycarbonate optical fiber core sensor.

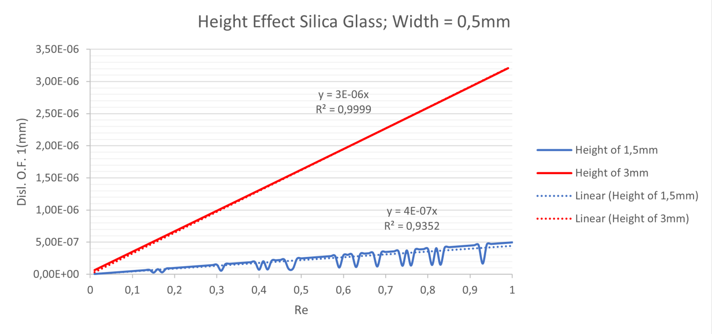

(c) Fixed width of 0.5 mm with 1.5 mm and 3 mm varying height for fused silica glass optical fiber core sensor.

Figure 3.8: Linear regression for tip displacement in the x-axis of the first optical fiber (from left to right) with the increase of the Reynolds number.

with $7 \cdot 10^{-5}$ m for its coefficient, slightly greater than $5 \cdot 10^{-5}$ mm coefficient from 0.5 mm thick and 3 mm high polycarbonate core sensor.

Thus, from the eight possible configurations presented, the one that presents the greatest tip displacement under different water flows, varying

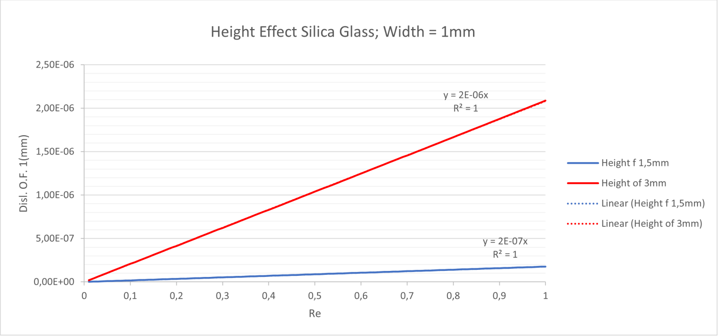

(d) Fixed width of 1 mm with 1.5 mm and 3 mm varying height for fused silica glass optical fiber core sensor.

Figure 3.8: Linear regression for tip displacement in the x-axis of the first optical fiber (from left to right) with the increase of the Reynolds number.

with the Reynolds number is the 3 mm height and 0.5 mm thick polycarbonate optical core sensor. Next, by choosing the geometry and the materials of this sensor as the best performing one in the parametric analysis, the expected phase difference created will be calculated, in the next section.

3.4 Expected Phase Difference Output

To calculated the expected phase difference for the sensor chosen in the latter section, we can use the equation (2.37),

$$\delta\phi \approx 2kn_0L(E_{22}^1 - E_{22}^2)\left[1 - \frac{Cn^2}{2}\right], \tag{3.2}$$

where k is the wavenumber, given by $k = \frac{2\pi}{\lambda}$, E_{22} is the strain along the fiber lenght n_0 is the original refractive index of the optical fibers, L is the length of the fibers (2.5 mm in this case) and C is given by [3] for polycarbonate as approximately 0.103. To perform the following calculations, the interferometer setup of [3] will be used, thus a He-Ne laser with wavelength of 632.8 nm and the refractive index of a polycarbonate optical fiber with PDMS cladding is taken to be approximately 1.5, as the polycarbonate fiber with PMMA cladding is 1.58 [3] and without cladding the polycarbonate fiber has its refractive index between to 1.57-1.59 [42]. The change in the expected phase difference calculated with 1.5 instead of 1.58 was negligible.

In COMSOL Multiphysics®, by selecting the E_{YY} component of the Green strain tensor for the material coordinates of each polycarbonate optical fiber inside the sensor, it is possible to plot the strain in the YY direction for each Reynolds number tested, as shown in figure 3.9.

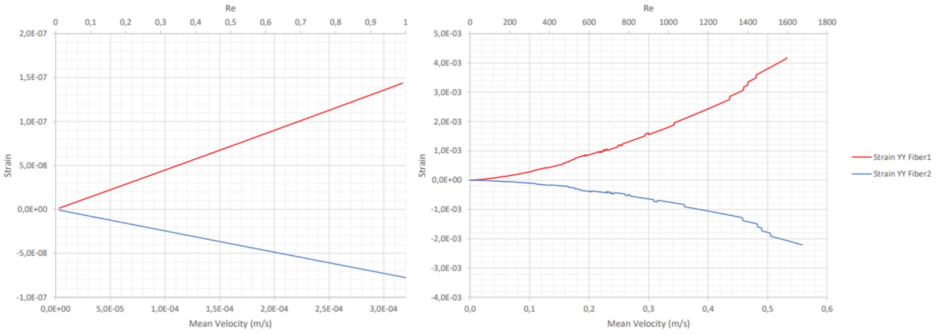

Figure 3.9: This figure shows two graphics, the first one at the left shows the Green strain of both optical fibers inside the sensor from $0.01 < Re < 1$, and the second shows the same information until $Re \approx 1600$. There are two x-axis, showing the Reynolds number (above) and the mean flow velocity (below).

Next, from the strain data of each sensor and utilizing the equation 3.2, it is possible to calculate the expected phase difference of this sensor, in this regime. To check the consistency of the data obtained, the expected phase difference is compared with an approximation proposed by [3], that relays on the tip-displacements (in the x-direction) of the sensor other than on the strains directly,

$$\Delta\phi \approx 8\pi n(1 - \frac{Cn^2}{2})(\frac{\delta}{L})(\frac{\Lambda}{\lambda}), \tag{3.3}$$

where Λ is the distance between the center of each optical fiber, which in the case of the sensor tested is 125 μm, δ is the tip displacement in the x-axis direction, which is presented in plot 3.7 and the other parameters were already explained in the beginning of this section. The expect phase difference output of the sensor is shown at figure 3.10.

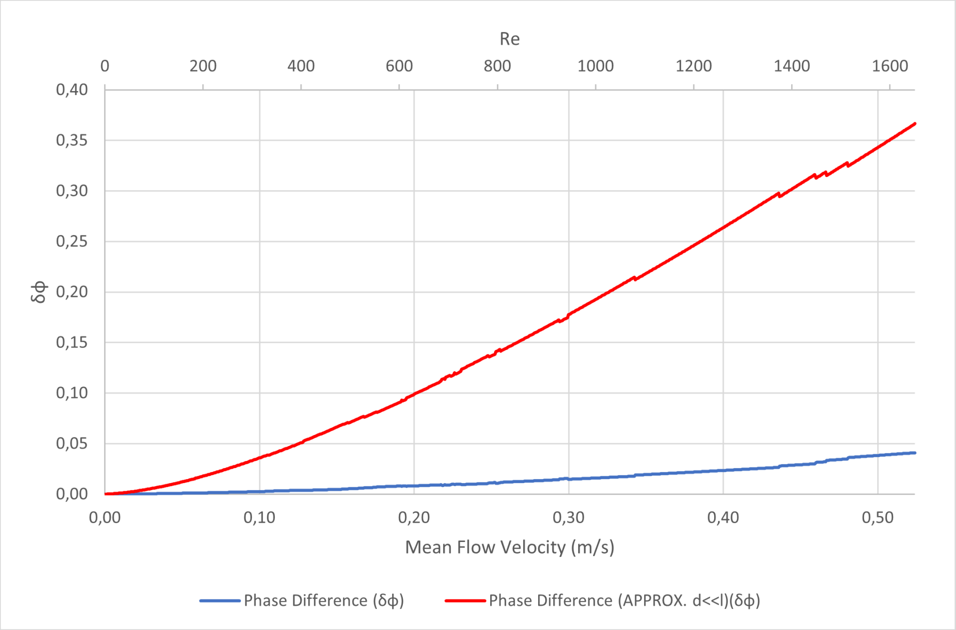

Figure 3.10: This figure shows the graphic of the theoretical phase difference for the small deformation approximation (red line) and for the numerically calculated 2D system (blue line), from $Re = 0$ until $Re \approx 1600$. There are two x-axis, showing the Reynolds number (above) and the mean flow velocity (below).

In figure 3.10 the maximum achieved phase difference was around 0,35 rad (more than $\pi/10$) for a water flow with mean flux velocity of 0.5 m/s and for the minimum, the graphic begins at 0 radians (undeformed sensor, with no water flux hitting it). The phase difference does not arrive to the minimum detectable phase difference of $\pi/5$ for a classical Michelson Interferometer [43] based on fringe detection, requiring a more sensible technique to perceive this order of phase difference. A suggestion would be to measure the intensity of the interference signal, which depends on the phase difference [44], which should be able to sense phase differences up to $\delta\phi = 10^{-3}$ [45].

For the 2D model, phase differences of $\delta\phi = 10^{-3}$ are achieved for $Re \approx 160$, and for the specific geometry of the channel of this thesis, for mean flow velocities of $V \approx 5.10^{-2} m/s$. If compared with the sensitivity of other sensors, such as the one from [19] with the detection limit threshold of 8 $\mu m/s$, it does not seem a sensible sensor, however the detection limit still depends on the interferometer utilized. With this said, this calculation is done with the intention to check for the viability of the hereby proposed sensor.

Coming up in chapter 4, the simulation of the behavior of this sensor, in a new 3D configuration, is studied in order to obtain a simulation that could relate more to a real-world application.

3.5 Summary

In this chapter the simulation parameters and materials properties are presented in section 3.1, such as the geometry of the proposed sensors, the physics packages used, the meshing performed by COMSOL, the boundary conditions and material mechanical properties. Next, in section 3.2, the results of the simulations are presented: the tip displacement of the eight sensor configurations, the graphics of how the sensor bent in each one of the simulations and the fluid behavior around and after the sensor (just the discussion, figures in appendix A), and then discussed. Finally a expected phase difference (section 3.10), output for the interferometric bending sensor is simulated numerically with the strain difference between the two optical fibers for all the values of the Reynolds number simulated.

From the results present in this chapter and appendix A it can be observed that the 1.5 mm height sensor have a good performance from the perspective of microfluidics, but also show a really low tip displacement, in the Angstrom scale, which is not ideal for the sensing applications. For this reason, yet having the best fluidics performance (not perturbing the laminar flow after the sensor), they cannot be chosen for the present flow sensing application, thus the 3 mm height PC optical core sensor is the chosen geometry and material.

Chapter 4

3D Sensor Simulations

In this section, the chosen sensor configuration from the parametric analysis (section 3.3) is modeled in a new 3D configuration.. Next, 3D laminar regime fluid-structure interaction simulations are performed in order to understand the mechanical behavior of this new 3D sensor, with focus on the displacement of the sensor, which is translated into a phase difference of the interferometer bending sensor afterwards.

4.1 Geometry and Dimensions of the proposed 3D sensor

The materials of the proposed 3D sensor are as the sensor picked from the parametric analysis: a PDMS cupula that follows the mechanical properties described in section 3.1 and in table 3.1, as well as the properties for the polycarbonate optical fibers that composes the two fiber core of the sensor. No further materials are introduced in the 3D geometry proposed sensor.

The proposed geometry, which is inspired in the sensor geometry of [2] (present in figure 1.1), intends to minimize the cross section in order to reduce the perturbations in the fluid flow after the sensor. Therefore, a rectangular cross section sensor with 20% of the width of the sensor proposed by [2] is introduced. This new geometry takes the same height of the sensor chosen in the parametric analysis (3 mm), with a dome in the tip (internal radius of 250 μm), with both width and depth of 500 μm. The optical fiber inside still have the same height of 2.5 mm, diameter of 125μm and are place symmetrically inside the PDMS cupula, line up in the direction of the

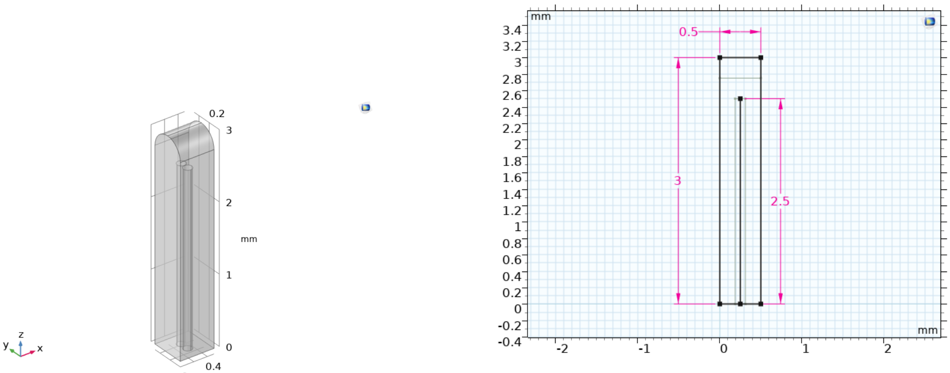

(a) Isometric view of the 3D sensor.

(b) Measures of the 3D sensor in the front view (cross section of xz plane).

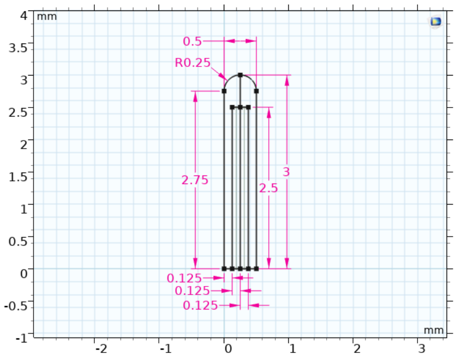

(c) Measures of the 3D sensor in a side view (cross section of the yz plane).

Figure 4.1: Geometries for the new proposed 3D interferometric flow sensor modeled in the COMSOL Multiphysics ® software [1]. All measures are given in millimeters.

flow. Figure 4.1 gives the precise measures and geometry of the sensor.

For the simulation parameters, all the packages from COMSOL Multiphysics® [1] that were used in section 3.1 in chapter 3 are used: fluid-structure interaction multiphysics package, laminar flow package and solid mechanics for elastic materials package. The channel is, once over, based on the channel by [2], with a squared cross section of 11.25 mm x 11.25 mm and a depth of 60 mm, with the sensor being place in the middle of the width of the bottom wall of the channel, and 20 mm distant from the inlet of fluid, as presented in figure 4.2.

The meshing for the 3D model was done in the same way explained in 3.1, with the finer free tetrahedral mesh preset performed by the Physics-Controlled mesh COMSOL internal function. The outlook of the meshing for the sensor and the channel can be observed in figure 4.3.

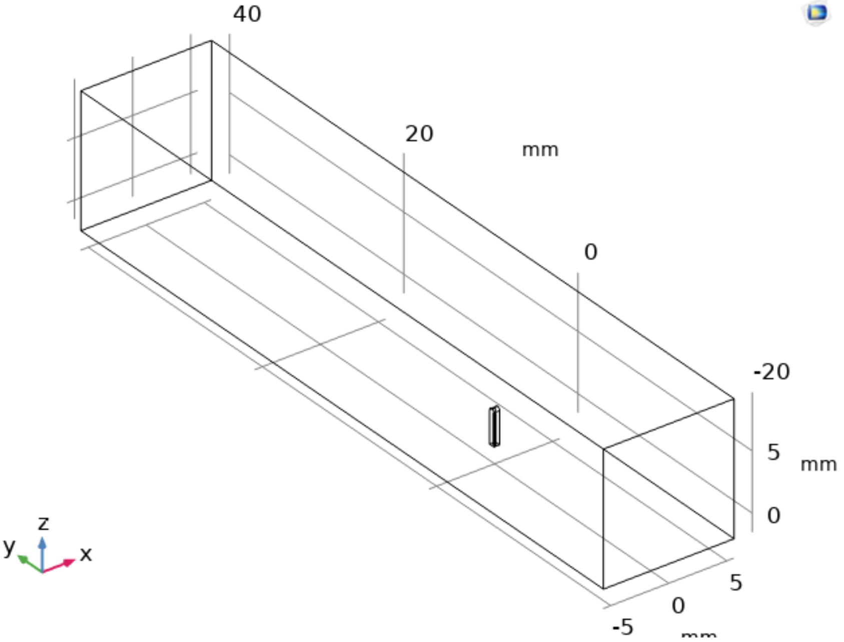

Figure 4.2: Diagram providing the dimensions (in millimeters) of the channel utilized in the fluid-structure interaction 3D simulations. Done with COMSOL Multiphysics® [1]

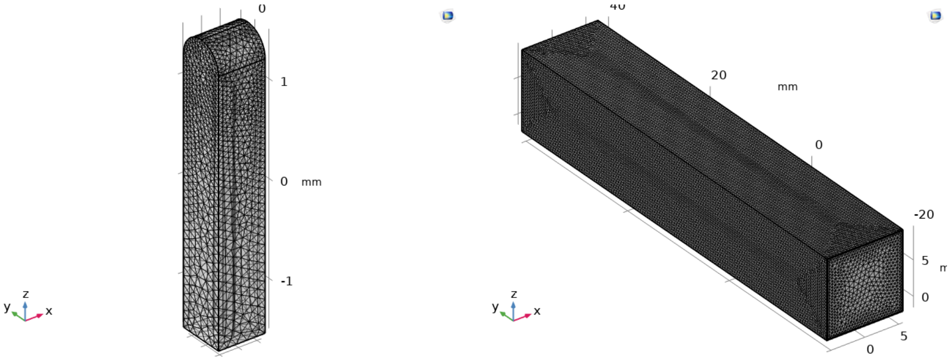

(a) Physics-controlled free tetrahedral mesh for 3D sensor.

(b) Physics-controlled free tetrahedral mesh for 3D channel.

Figure 4.3: Meshing outlook in COMSOL, with finer preset selected in Multiphysics® [1].

The internal configuration of the sensor, regarding the fiber-PDMS interface, still relies on a contact pair between both (assembly), which is set to be a adhesion interface with the gap between the fiber and the cupula equals to zero, for the same reason mentioned in section 3.1. The line of contact between the optical fiber cylinders is modeled as a contact pair in

COMSOL, with friction, carrying the same coefficient used in the 2D simulations for the PC-PC interaction (table 3.2). On the bottom of the sensor (figure 4.4 are placed the fixed boundary conditions, that fixes the sensor to the bottom wall of the channel. And, finally, the slip condition for the laminar fluid flow is taken to be a no-slip condition, as explained in more detail in section 3.1.

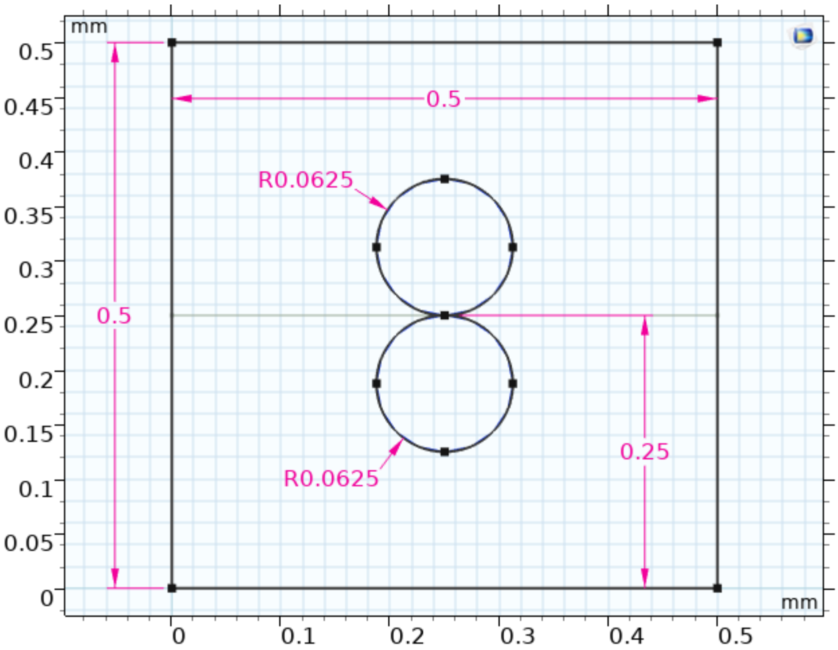

Figure 4.4: Diagram providing the dimensions (in millimeters) of the bottom part for the sensor, in which are applied the fixed boundary conditions. The view is from the xy cross section. Done with COMSOL Multiphysics® [1]

4.2 Fluid-Structure Interaction Results and Discussion

In this section the fluid-structure interaction simulations of the new proposed 3D sensor configuration will be presented alongside with the graphics of tip displacement - in the y-direction, with is parallel to the flow direction - and the graphic of the strain in each fiber.

To analyze its behavior, 150 simulations were performed in the laminar regime from $Re = 0.01$ until $Re = 2000$, equally divided into same value intervals of the Reynolds numbers. As the simulations presented in the previous chapter, the simulation each Reynolds number is independent and performed in stationary state. The reduced number of simulation with relation to the two-dimensional simulations is due to fact that the three-dimensional simulations are much more time consuming than the two-dimensional ones,each 150 simulations took 2 days approximately, compared with 8800 2D simulations that took the same two days.

As state in chapter 3, in section 3.2, the results aimed to be achieved are the tip-displacement in the y direction (direction of the flow in the three-dimensional simulation) and the behavior of the fluid around and after the sensor. In appendix B the fluid velocity magnitude (figure B.1) shows that, as present in the two-dimensional study, the $Re = 1$ flow passes gently around the sensor, creating no perturbation in the laminar regime other than around the own structure of the sensor, but returning this small distortion to the original flow immediately after it (subfigures B.1a and B.1b). For the edge of the laminar regime, when the Reynolds number $Re = 2000$, in subfigures B.1c and B.1d it is possible to observe that the flow does not return to its original form after the sensor. An area of low velocity is created behind the sensor, thus perturbing the flow. This geometry seems to perturb the laminar regime flow when the Reynolds number is at high values, confirming with the 3D simulation what was first visualized in the 2D simulation of the same height and width.

The displacement of the sensor under various flow velocities can be visualized at graphic 4.6, in which the quadratic relation between the tip displacement is clear, confirming the theoretical prediction of [2]. The maximum displacement is also greater then the one predict in the 2D simulations, in the order of micrometers. The sensor itself at $Re = 2000$ can be visualized at figure 4.5, where the mechanical cantilever behavior under a distributed load can be observed.

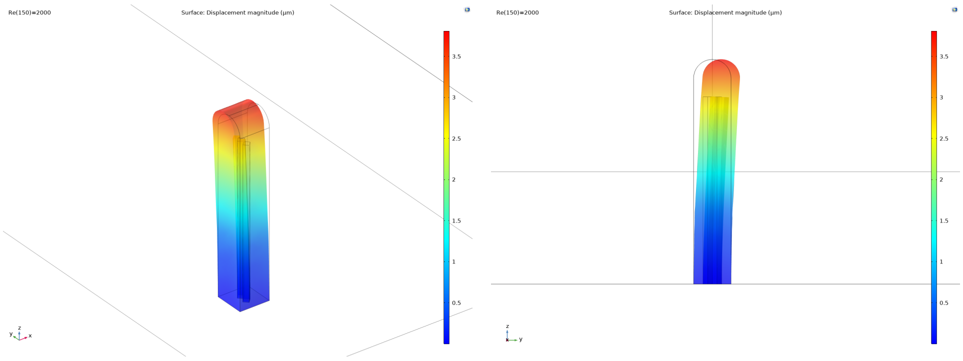

(a) PC twin core sensor with 1.5 mm of height and 0.5 mm of width.

(b) PC twin core sensor with 1.5 mm of height and 1 mm of width.

Figure 4.5: Sensor displacement magnitude, for 3D sensor, under laminar water flow at $Re = 2000$. *Simulations and graphics done in COMSOL Multiphysics* ® *software [1].*

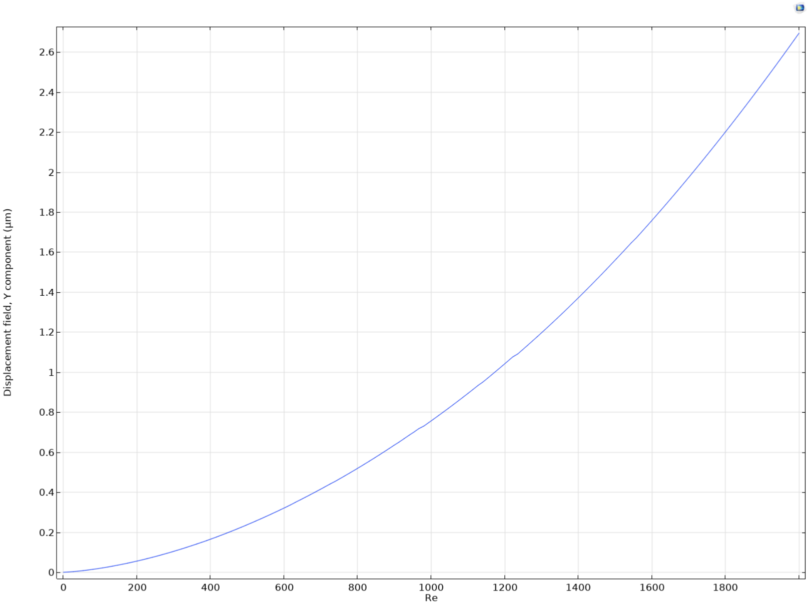

Figure 4.6: Tip displacement in the y direction (parallel to the flow) plot of the top of the first optical fiber inside the 3D sensor, for each Reynolds number simulation. Done with COMSOL Multiphysics® [1].

4.3 Expected Phase Difference Output

In order to do the same procedure as in section 3.4, the strain inside each one of the optical fibers is plotted against the Reynolds number of the flow, in graphic 4.7.

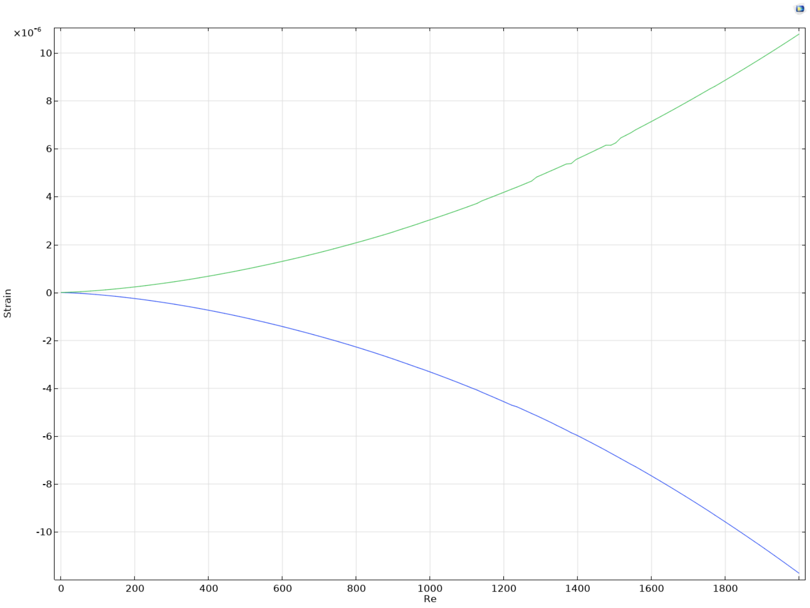

Figure 4.7: Strains of each polycarbonate optical fiber inside the sensor plot for each Reynolds number simulation. Done with COMSOL Multiphysics® [1].

The value of the strain in each fiber is three orders of magnitude less than the strain observed in the same 2D sensor, although the tip displacement is one order of magnitude greater in the 3D sensor. This behavior can be explained by greater freedom of movement that the fibers have inside the 3D configuration, with just a line of contact providing friction contact between the fibers, in the other hand, in the 2D model the fibers are in constant contact with each other, hence making the sensor to be less compliant and inducing more strain in the fibers. One possible solution, to increase the strain in the fibers is to glue the fibers inside the 3D sensor.

This deviation from the unified bending of the structure can be clearly observed in the expected phase difference output, graphic 4.8, which compares the small deflection approximation when $d << L$ (red line in graphic 4.8), that assumes that the beam in deforming altogether and the real phase difference output (blue line in graphic 4.8).

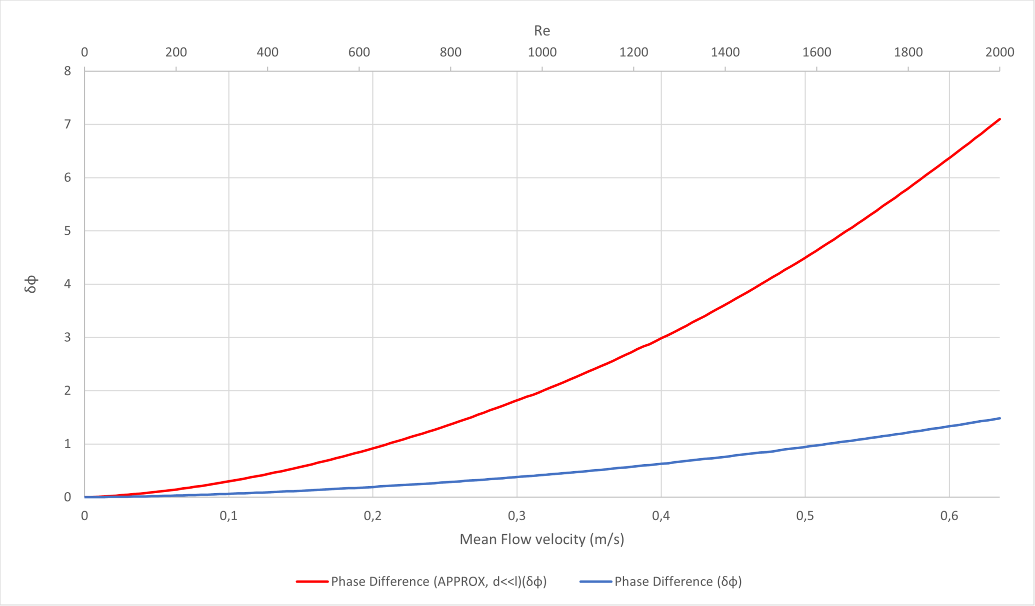

Figure 4.8: This graphic plots the expected phase difference in the optical interferometer due to the bending of the two optical fiber inside the PDMS cupula, firstly for the small deformation approximation ($d << L$, red line), than to the real strain observed in the fluid-structure interaction (blue line).

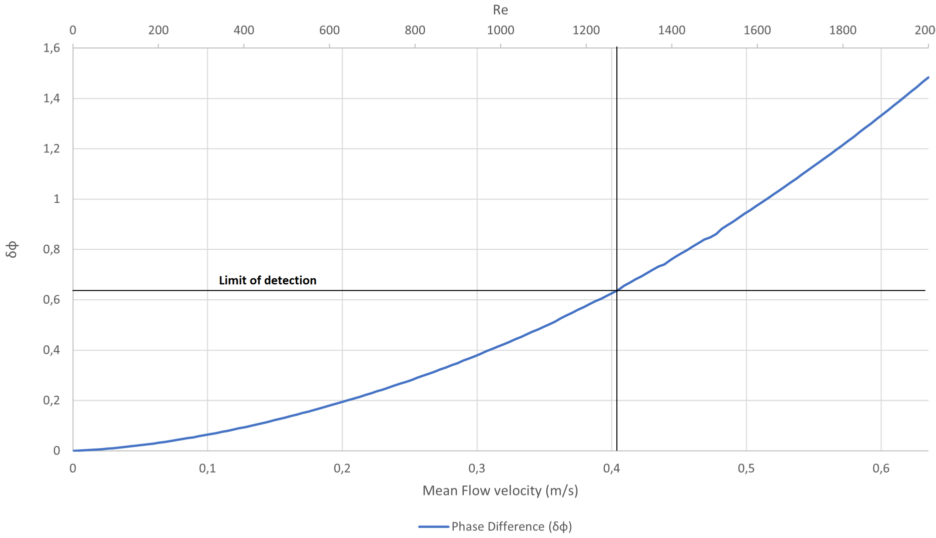

Figure 4.9: This graphic plots the expected phase difference in the optical interferometer due to the bending of the two optical fiber inside the PDMS cupula and showing with the two black lines the limit of detection of the fringe interferometric sensing technique.

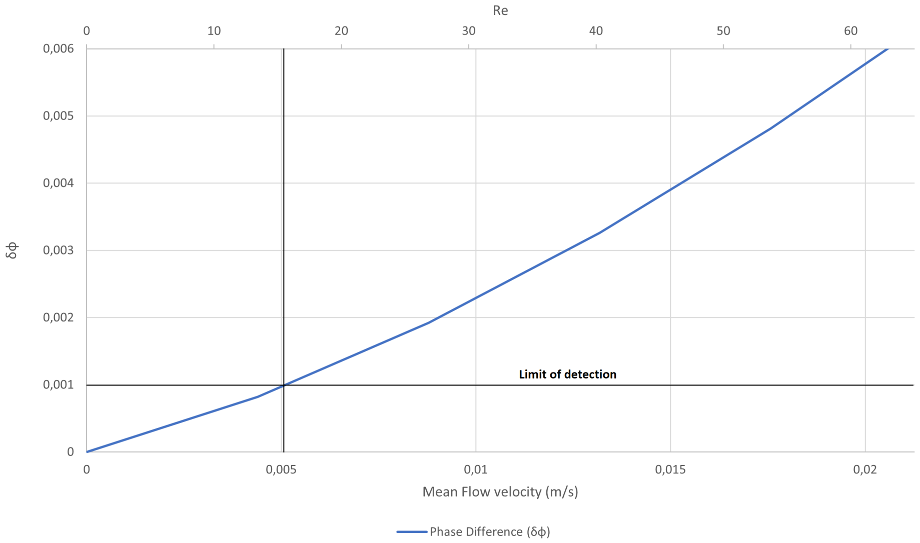

Figure 4.10: This graphic plots the expected phase difference in the optical interferometer due to the bending of the two optical fiber inside the PDMS cupula and showing with the two black lines the limit of detection of the intensity of the interference signal.

It is observed that the phase difference calculated from the strains gets to the value of 1.6 radians at the edge of the laminar regime, passing by the threshold of detection ($\pi/5$) for the fringe detection method around $Re = 1200$ (graphic in figure 4.9). On the other hand this threshold of detection for the small deflection approximation is around $Re = 300$, showing a big difference between the column deflecting altogether and the sensor with two independent optical fibers.

The other adopted detection technique, which is given by the measure the intensity of the interference signal, in figure 4.10, which depends on the phase difference [44], mentioned in section 3.4 of 3, is achieved with $Re = 15$, giving more precise measuring of the laminar mean velocity flow, than the previous technique.

For the fringe detection method, the threshold of detection the proposed sensor is around 0.4 m/s of mean flow velocity, which is several orders of magnitude higher than other alternatives, such as the sensor proposed by Asadnia et al. [19], which has the threshold of detection of 8 μm. Nonetheless, the intensity of the interference signal measuring method can give a lower value of threshold detection with respect to the fringe counting method, as low as $V \approx 5 * 10^{-3}$ ($Re \approx 15$), which points to a more sensitive system that would work in all the laminar regime, from the threshold of detection.

4.4 Summary

In this chapter, the geometry of the new 3D sensor is introduced with the simulation parameters in section 4.1. Next, in section 4.2, the results of the simulations are presented: the tip displacement of the 3D sensor, the graphics of how the sensor bent in each one of the simulations and the fluid behavior around and after the sensor (just the discussion, figures in appendix B), and then discussed. Finally a expected phase difference (section 4.3), output for the interferometric bending sensor is simulated numerically with the strain difference between the two optical fibers for all the values of the Reynolds number simulated.

It is observed in this chapter that the tip displacement is greater than the one observed in the 2D simulation for the same geometry. In the 2D simulations the tip displacement arrived until, approximately, 0.14 μm for $Re \approx 1650$, while in this 3D simulation the tip displacement was of 1.9μ for $Re \approx 1650$. This behavior could be described by the plane stress condition imposed in the 2D simulations, which could affect the output of the final strain, as the plane stress equations are different (they don't include the σ_x, x-axis referenced on Figure 4.3) than the ones in the Generalized Hooke Law.

Chapter 5

Conclusion and Future Directives

This work has provided results of the mechanical behavior of a compliant PDMS cupula sensor with a two-core optical fiber interferometric system for a series of steady state fluid-structure interaction simulations performed for laminar regime, in the interval $0.01 < Re < 2000$. Two-dimensional simulations were performed for 8 different configurations of sensors, which varied in height, width and the material of the optical fibers inside the sensor, being, thus, two different heights, two different widths and two different materials for the optical fibers. From the results of these simulations, a parametric analysis was performed utilizing a linear regression model on how the amount of tip displacement of the first optical fiber varies with the Reynolds number for small displacements. This analysis showed that the sensor with 3 mm of height, 0.5 mm in width and polycarbonate as the material for the optical fiber part, was the more inclined to bend with the increase in the water flux, thus being the most suited configuration for a sensor. On the other hand, the analysis of the velocity magnitudes for all 2D simulations showed that the sensors with 1 mm of height do not perturb the flow after the sensor itself - just right on the top of it - while the ones with 3 mm of height tend to perturb it further. Nonetheless, the tip deflection for all 1 mm sensors are in the order of magnitude of Angstroms, fact that does not permit this geometry to be a good sensing one.

From this first selection, a 3D model was constructed utilizing the same parameters of the previously selected 2D model, and setting the depth of the sensor equal to the width. The same steady state laminar regime simulations were performed for this 3D sensor. From the results, it can be observed a great deviation in the strains in the fibers from the modeled independent fibers with friction adopted in between them and the single column adopted in the small deflection approximation, causing the difference in strain between the fibers be smaller in the free fibers than in the small deflection approximation solutions. From this result, a future directive would be to simulate numerically the fibers glued together or held inside a PMMA matrix like presented in [3]. Nonetheless, the interval of measurement in the laminar regime of the proposed sensor covers from $Re \approx 1200$ ($V \approx 0.4m/s$ for the presented duct) for the fringe detection interferometric measuring technique until $Re = 2000$, and for the interference signal intensity measuring technique the interval is larger, from $Re \approx 15$ ($V \approx 5 \cdot 10^{-3}m/s$ for the presented duct) until $Re = 2000$.

Other future improvement of the present work would be to present dynamic simulations of the sensor in a fluid-structure simulation, to understand how the vortexes created after the sensor could affect its behavior in a long duration setup.

Overall, the proposed sensor showed promising initial results, having its viability numerically tested for laminar regime water fluxes in a squared cross section duct. Further numerical analysis, such as the ones proposed in this chapter, and laboratory testing are required to test the sensor in real working conditions.

Bibliography

[1] COMSOL Multiphysics® v. 5.4. www.comsol.com. COMSOL AB, Stockholm, Sweden.

[2] James P. Wissman, Kaushik Sampath, Simon E. Freeman, and Charles A. Rohde. Capacitive bio-inspired flow sensing cupula. *Sensors (Switzerland)*, 2019.

[3] H. Qu, G. F. Yan, and M. Skorobogatiy. Interferometric fiber-optic bending/nano-displacement sensor using plastic dual-core fiber. *Optics Letters*, 39:4835, 8 2014.

[4] Elena Lurie-Luke. Product and technology innovation: What can biomimicry inspire? *Biotechnology Advances*, 32:1494–1505, 12 2014.

[5] Olusegun Aanuoluwapo Oguntona and Clinton Ohis Aigbavboa. Benefits of biomimicry adoption and implementation in the construction industry. In *International Conference on Applied Human Factors and Ergonomics*, pages 506–514. Springer, 2018.

[6] Qilong Zhao, Yunlong Wang, Huanqing Cui, and Xuemin Du. Bioinspired sensing and actuating materials. *Journal of Materials Chemistry C*, 7:6493–6511, 2019.

[7] Brian Dean and Bharat Bhushan. Shark-skin surfaces for fluid-drag reduction in turbulent flow: a review. *Philosophical Transactions of the Royal Society A: Mathematical, Physical and Engineering Sciences*, 368(1929):4775–4806, 2010.

[8] DS Barrett, MS Triantafyllou, DKP Yue, MA Grosenbaugh, and MJ Wolfgang. Drag reduction in fish-like locomotion. *Journal of Fluid Mechanics*, 392:183–212, 1999.

[9] J. Tové Martin. *An Introduction to the Visual System.* Cambridge university Press, 1996.

[10] Fred Delcomyn. From insect sense organs to biomimetic walking robots [exploratory dsp]. *IEEE Signal Processing Magazine*, 25(1):134–137, 2007.

[11] Nannan Chen, Craig Tucker, Jonathan M. Engel, Yingchen Yang, Saunvit Pandya, and Chang Liu. Design and characterization of artificial haircell sensor for flow sensing with ultrahigh velocity and angular sensitivity. *Journal of Microelectromechanical Systems*, 16:999–1014, 10 2007.

[12] John C. Montgomery, Cindy F. Baker, and Alexander G. Carton. The lateral line can mediate rheotaxis in fish. *Nature*, 389, 1997.

[13] Alfons B.A. Kroese, Johan M. Van der Zalm, and Joep Van den Bercken. Frequency response of the lateral-line organ of xenopus laevis. *Pflügers Archiv European Journal of Physiology*, 375, 1978.

[14] Alexander G. Carton and John C. Montgomery. A comparison of lateral line morphology of blue cod and torrentfish: Two sandperches of the family pinguipedidae. *Environmental Biology of Fishes*, 70, 2004.

[15] Michael E. McConney, Nannan Chen, David Lu, Huan A. Hu, Sheryl Coombs, Chang Liu, and Vladimir V. Tsukruk. Biologically inspired design of hydrogel-capped hair sensors for enhanced underwater flow detection. *Soft Matter*, 5:292–295, 2009.

[16] Adrian Klein and Horst Bleckmann. Determination of object position, vortex shedding frequency and flow velocity using artificial lateral line canals. *Beilstein Journal of Nanotechnology*, 2:276–283, 2011.

[17] JB Stocking, WC Eberhardt, YA Shakhsheer, BH Calhoun, JR Paulus, and M Appleby. A capacitance-based whisker-like artificial sensor for fluid motion sensing. In *SENSORS, 2010 IEEE*, pages 2224–2229. IEEE, 2010.

[18] M. Bora, A. G.P. Kottapalli, J. M. Miao, and M. S. Triantafyllou. Fish-inspired self-powered microelectromechanical flow sensor with biomimetic hydrogel cupula. *APL Materials*, 5, 10 2017.

[19] Mohsen Asadnia, Ajay Giri Prakash Kottapalli, K. Domenica Karavitaki, Majid Ebrahimi Warkiani, Jianmin Miao, David P. Corey, and Michael Triantafyllou. From biological cilia to artificial flow sensors: Biomimetic soft polymer nanosensors with high sensing performance. *Scientific Reports*, 2016.

[20] Tateo Shimozawa, Jun Murakami, and Tsuneko Kumagai. Cricket wind receptors: thermal noise for the highest sensitivity known, 2003.

[21] Sietse M. Van Netten. Hydrodynamic detection by cupulae in a lateral line canal: Functional relations between physics and physiology. *Biological Cybernetics*, 94, 2006.

[22] Horst Bleckmann. Journal of comparative physiology. a reaction time and stimulus frequency in prey localization in the surface-feeding fish aplocheilus iineatus. *J. Comp. Physiol*, 140:163–172, 1980.

[23] Yu Zhao, Julien Perchoux, Lucie Campagnolo, Thierry Camps, Reza Atashkhooei, and Véronique Bardinal. Optical feedback interferometry for microscale-flow sensing study: numerical simulation and experimental validation. *Optics Express*, 24:23849, 10 2016.

[24] Lucie Campagnolo, Milan Nikolić, Julien Perchoux, Yah Leng Lim, Karl Bertling, Karine Loubière, Laurent Prat, Aleksandar D. Rakić, and Thierry Bosch. Flow profile measurement in microchannel using the optical feedback interferometry sensing technique. *Microfluidics and Nanofluidics*, 14:113–119, 1 2013.

[25] Elizabeth Carr, Eleanor C. Mackle, Malcom C. Finlay, Charles A. Mosse, Joanna M. Coote, Ioannis Papakonstantinou, and Adrien E. Desjardins. Optical interferometric temperature sensors for intravascular blood flow measurements. volume Part F142-ECBO 2019. OSA - The Optical Society, 2019.

[26] Khurram Naeem, Youngjoo Chung, and Il Bum Kwon. Highly sensitive two-dimensional bending vector sensor using an elliptic two-core pcf. *IEEE Photonics Technology Letters*, 30:273–276, 2 2018.

[27] Joel Villatoro, Amy Van Newkirk, Enrique Antonio-Lopez, Joseba Zubia, Axel Schülzgen, and Rodrigo Amezcua-Correa. Ultrasensitive vec-

tor bending sensor based on multicore optical fiber. *Optics Letters*, 41:832, 2 2016.

[28] Properties of polycarbonate rods. Found in the website: http://www.goodfellow.com/e/polycarbonate.html. Accessed in 08/06/2021.

[29] Physical properties of corning 7940 fused silica glass. Found in the website: http://valleydesign.com/7940.ht. Accessed in 08/06/2021.

[30] Réal Vallée and Denis Drolet. Practical coupling device based on a two-core optical fiber. *Applied optics*, 33(24):5602–5610, 1994.

[31] Ellad B. Tadmor, Ronald E. Miller, and Ryan S. Elliott. *Continuum mechanics and thermodynamics: From fundamental concepts to governing equations*, volume 9781107008267. 2011.

[32] Ted Belytschko, Wing Kam Liu, Brian Moran, and Khalil I. Elkhodary. *Nonlinear Finite Element for Continua and Structures.* Wiley, second edition edition, 2014.

[33] Cláudio Geraldo Schön. Editora Campus. SCHON, C. G. (2013). Mecânica dos materiais: fundamentos e tecnologia do comportamento mecânico. Editora Campus. 1ª ed.

[34] Mikkel Wennemoes Hvitfeld. *General rights Effective modelling of acoustofluidic devices.* PhD dissertation, Technical University of Denmark, 2017.

[35] Angelina Müller, Matthias C. Wapler, and Ulrike Wallrabe. A quick and accurate method to determine the poisson's ratio and the coefficient of thermal expansion of pdms. *Soft Matter*, 15:779–784, 2019.

[36] D. Armani, C. Liu, and N. Aluru. Re-configurable fluid circuits by pdms elastomer micromachining. *Technical Digest. IEEE International MEMS 99 Conference. Twelfth IEEE International Conference on Micro Electro Mechanical Systems (Cat. No.99CH36291)*, 1999.

[37] Alfredo Pinelli, Markus Uhlmann, Atsushi Sekimoto, and Genta Kawahara. Reynolds number dependence of mean flow structure in square duct turbulence. *Journal of Fluid Mechanics*, 644:107–122, 2 2010.

[38] Mitsubishi engineering-plastics corporation - physical properties of iupilon/novarex (PC) - technical data sheet.

[39] Ramin Mirzazadeh and Stefano Mariani. Estimation of air damping in out-of-plane comb-drive actuators. *Micromachines*, 10, 4 2019.

[40] Filip Petersson, Andreas Nilsson, Cecilia Holm, Henrik Jönsson, and Thomas Laurell. Continuous separation of lipid particles from erythrocytes by means of laminar flow and acoustic standing wave forces. *Lab on a Chip*, 5:20–22, 2005.

[41] Andreas Lenshof and Thomas Laurell. Continuous separation of cells and particles in microfluidic systems. *Chemical Society Reviews*, 39:1203–1217, 2 2010.

[42] Andrea Fasano, Getinet Woyessa, Pavol Stajanca, Christos Markos, Alessio Stefani, Kristian Nielsen, Henrik K Rasmussen, Katerina Krebber, and Ole Bang. Fabrication and characterization of polycarbonate microstructured polymer optical fibers for high-temperature-resistant fiber bragg grating strain sensors. *Optical Materials Express*, 6(2):649–659, 2016.

[43] Silvano Donati. *Electro-optical instrumentation: sensing and measuring with lasers.* Pearson Education, 2004.

[44] Douglas T Smith, Jon R Pratt, and LP Howard. A fiber-optic interferometer with subpicometer resolution for dc and low-frequency displacement measurement. *Review of Scientific Instruments*, 80(3):035105, 2009.

[45] David Krohn. Fiber optic sensors:fundamentals and applications. 2015.

[46] Zhifang Fan, Jack Chen, Jun Zou, David Bullen, Chang Liu, and Fred Delcomyn. Design and fabrication of artificial lateral line flow sensors. *Journal of micromechanics and microengineering*, 12(5):655, 2002.

[47] Hong Lei, Montassar Aidi Sharif, Derek A. Paley, Matthew J. McHenry, and Xiaobo Tan. Performance improvement of ipmc flow sensors with a biologically-inspired cupula structure. volume 9798, page 979827. SPIE, 4 2016.

Appendix A

Velocity Magnitude Profiles of 2D simulations

In this appendix the fluid behavior around and after the sensor in the channel is illustrated. All the fluid 2D simulations are presented in a profile view, for the values of the Reynolds number 1 and the maximum achieved for the simulations (always equal or minor to 2000).

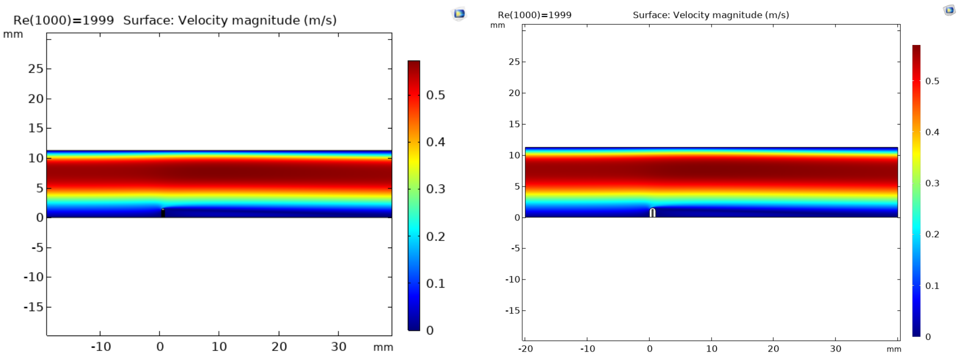

(a) $Re = 1999$ in laminar flow. Dimensions and geometry of the fused silica glass twin core 2D sensor with 1.5 mm of height and 0.5 mm of width.

(b) $Re = 1999$ in laminar flow. Dimensions and geometry of the fused silica glass twin core 2D sensor with 1.5 mm of height and 1 mm of width.

Figure A.1: Flow velocity magnitude in the channel, for sensors for the maximum Reynolds number achieved in each simulation, under laminar water flow. Simulations and graphics done in COMSOL Multiphysics ® software [1].

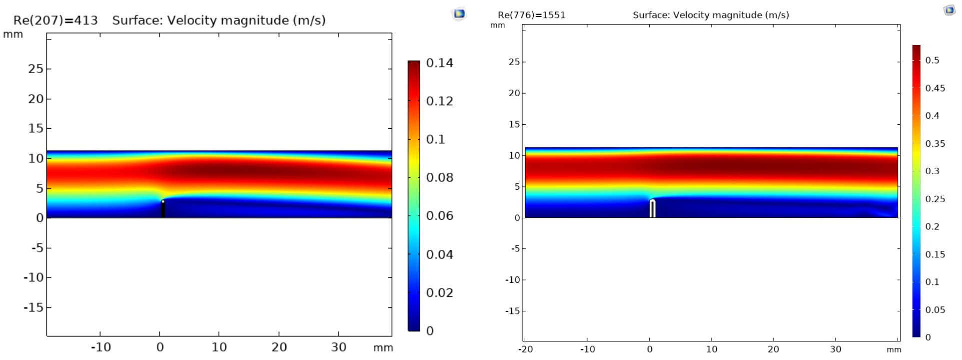

(c) $Re = 413$ in laminar flow. Dimensions and geometry of the fused silica glass twin core 2D sensor with 3 mm of height and 0.5 mm of width.

(d) $Re = 1551$ in laminar flow. Dimensions and geometry of the fused silica glass twin core 2D sensor with 3 mm of height and 1 mm of width.

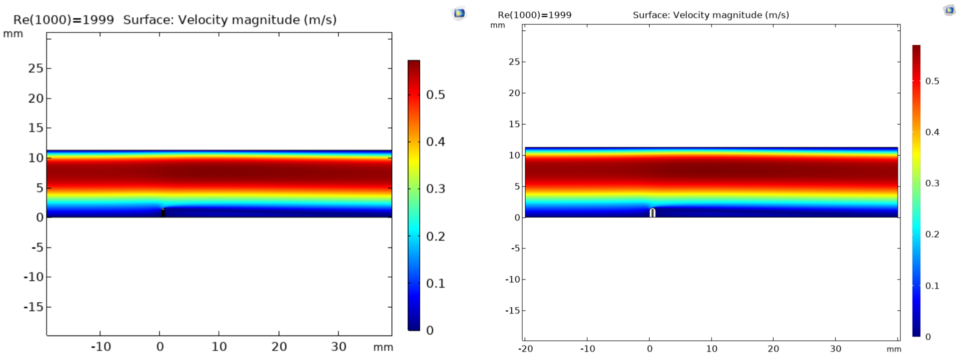

(e) $Re = 1999$ in laminar flow. Dimensions and geometry of the polycarbonate optical fiebr twin core 2D sensor with 1.5 mm of height and 0.5 mm of width.

(f) $Re = 1999$ in laminar flow. Dimensions and geometry of the polycarbonate optical fiebr twin core 2D sensor with 1.5 mm of height and 1 mm of width.

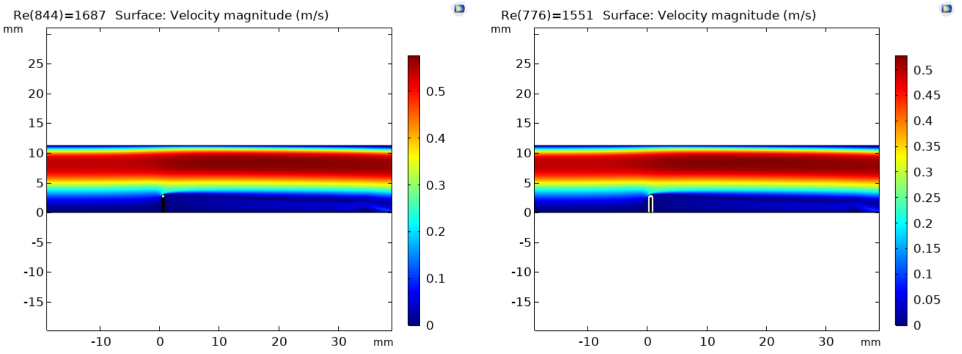

(g) $Re = 413$ in laminar flow. Dimensions and geometry of the polycarbonate optical fiebr twin core 2D sensor with 3 mm of height and 0.5 mm of width.

(h) $Re = 1551$ in laminar flow. Dimensions and geometry of the polycarbonate optical fiebr twin core 2D sensor with 3 mm of height and 1 mm of width.

Figure A.1: Flow velocity magnitude in the channel, for sensors for the maximum Reynolds number achieved in each simulation, under laminar water flow. Simulations and graphics done in COMSOL Multiphysics ® software [1].

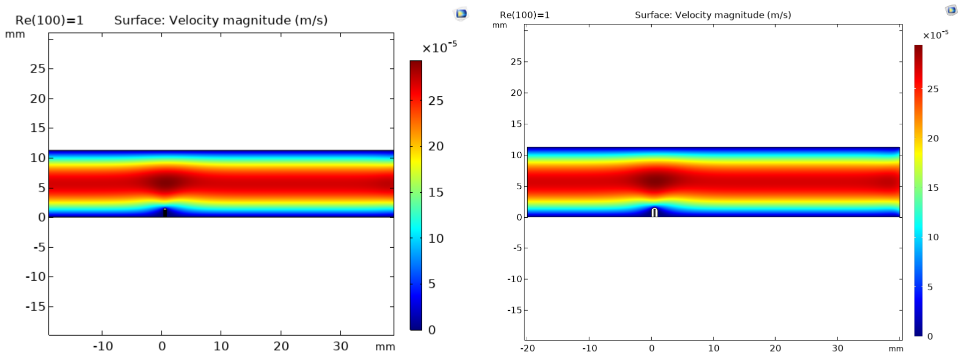

(a) Dimensions and geometry of the fused silica twin core optical fiber 2D sensor with 1.5 mm of height and 0.5 mm of width.

(b) Dimensions and geometry of the fused silica twin core optical fiber 2D sensor with 1.5 mm of height and 1 mm of width.

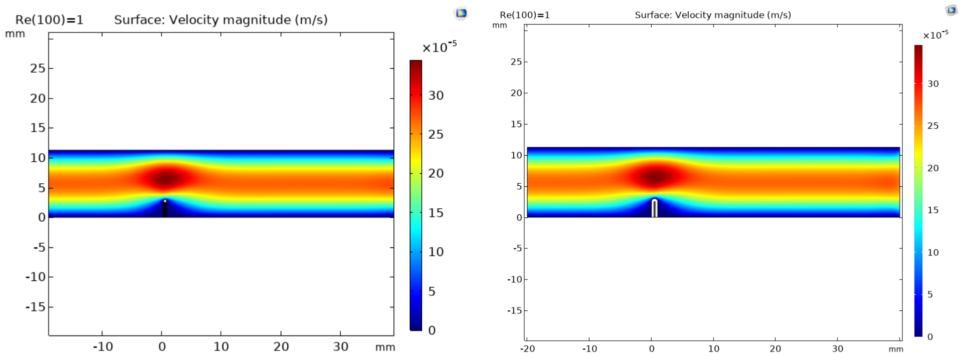

(c) Dimensions and geometry of the fused silica twin core optical fiber 2D sensor with 3 mm of height and 0.5 mm of width.

(d) Dimensions and geometry of the fused silica twin core optical fiber 2D sensor with 3 mm of height and 1 mm of width.

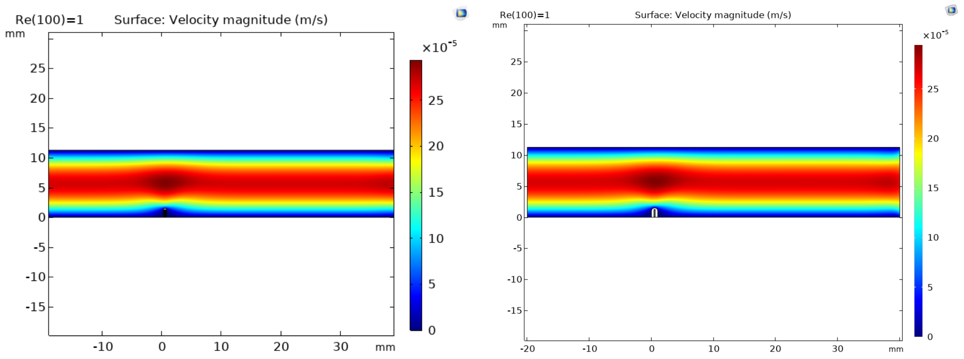

(e) Dimensions and geometry of the polycarbonate twin core optical fiber 2D sensor with 1.5 mm of height and 0.5 mm of width.

(f) Dimensions and geometry of the polycarbonate twin core optical fiber 2D sensor with 1.5 mm of height and 1 mm of width.

Figure A.2: Flow velocity magnitude in the channel, for sensors for $Re = 1$ under laminar water flow. Simulations and graphics done in COMSOL Multiphysics ® software [1].

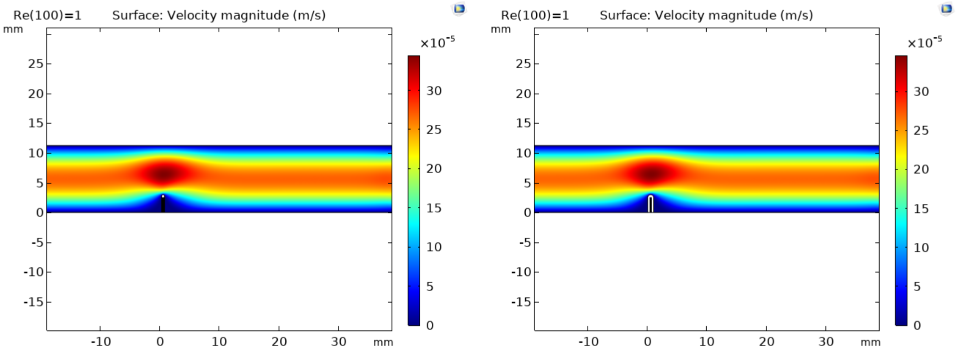

(g) Dimensions and geometry of the polycarbonate twin core optical fiber 2D sensor with 3 mm of height and 0.5 mm of width.

(h) Dimensions and geometry of the polycarbonate twin core optical fiber 2D sensor with 3 mm of height and 1 mm of width.

Figure A.2: Flow velocity magnitude in the channel, for sensors for $Re = 1$ *under laminar water flow. Simulations and graphics done in COMSOL Multiphysics* ® *software [1].*

Appendix B

Velocity Magnitude Profiles of 3D simulations

In this appendix the fluid behavior around and after the sensor in the channel is illustrated. The 3D fluid simulations are presented in a profile view, for the values of the Reynolds number 1 and 2000.

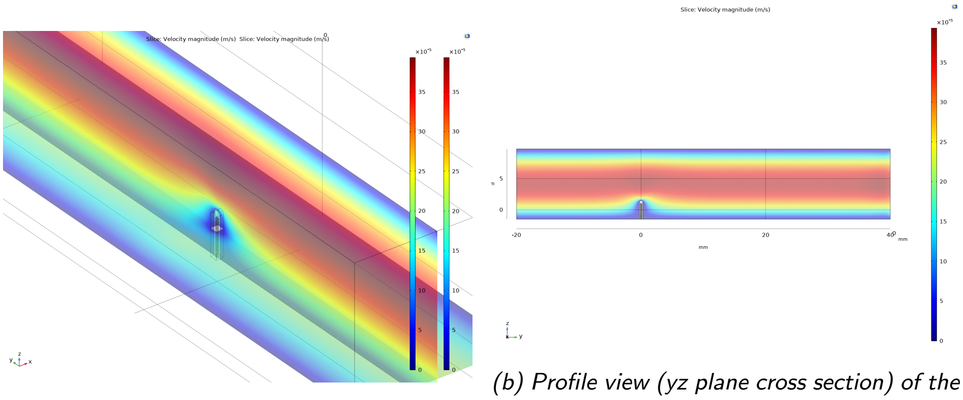

(a) Isometric view of the channel with the sensor under a flow of $Re = 1$.

(b) Profile view (yz plane cross section) of the channel with the sensor under a flow of $Re = 1$.

Figure B.1: Flow velocity magnitude in the channel, for 3D sensor for Reynolds numbers of $Re = 1$ and $Re = 2000$, under laminar regime water flow. Simulations and graphics done in COMSOL Multiphysics ® software [1].

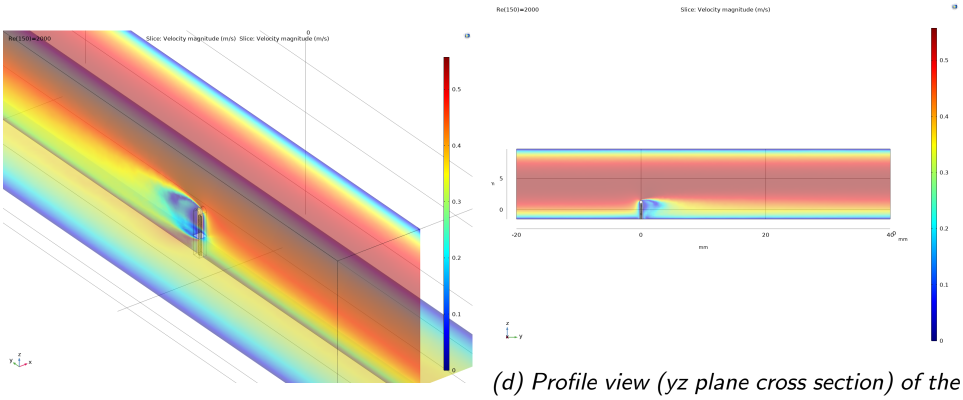

(c) Isometric view of the channel with the sensor under a flow of $Re = 2000$.

(d) Profile view (yz plane cross section) of the channel with the sensor under a flow of $Re = 2000$.

Figure B.1: Flow velocity magnitude in the channel, for 3D sensor for Reynolds numbers of $Re = 1$ and $Re = 2000$, under laminar regime water flow. Simulations and graphics done in COMSOL Multiphysics ® software [1].